S-Pol Data from PRECIP22

Example Signatures



Locals enjoying the sight of S-Pol. Picture by Mike Dixon.

Time to relax and ruminate

John C. Hubbert with contributions from Mike Dixon
Questions about this report? email hubbert@ucar.edu

This report contains a few examples of interesting polarimetric signatures from PRECIP22

National Center for Atmospheric Research





NCAR

17 August 2022

Contents

1 Introduction **1**

1.1 Operating Frequency and Antenna Patterns 1

2 Clutter Environment **2**

3 RHIs of a Large Convective Cell **10**

4 Meiyu Front and Multi-path Reflections **10**

5 Chaff Polarimetric Signatures **15**

6 Scatter from Ships in the Taiwan Strait **21**

7 Anomalous Propagation (AP) Clutter **24**

8 Insect Scatter and Behavior in Taiwan **28**

9 Sidelobe Bias Effects **34**

9.1 RHI Case 34

9.2 PPI Case, 4° Elevation 35

9.3 PPI Case 0.5° Elevation 39

10 Sea Clutter and Waves **39**

11 Bragg Scatter **39**

12 Aligned Ice Crystals Above the Melting Layer **44**

1 Introduction

As with each new S-Pol field campaign location, the Hsinchu, Taiwan deployment next to the ocean presented new (to S-Pol), interesting dual-polarimetric scattering signatures and herein, some of these are documented for reference for interested users of PRECIP data.

S-Pol itself made several firsts for this campaign. Due to supply chain issues, the fast transmit switch was not available so S-Pol operated in simultaneous H and V transmit mode. In order to extend the unambiguous range and velocity, the staggered PRT technique was used. This provided unambiguous echoes out to 240 km and unambiguous velocities of $\pm 28\,\mathrm{m\,s^{-1}}$.

Fluctuating transmit power was noticed in early to mid June and the transmitter pulse shaper unit was the culprit. CWB operates a NEXRAD style radar and they generously loaned us a new unit. These NEXRAD stock pulse shapers can only adjust the pulse width down to 1.5 μs while S-Pol normally operates with a 1 μs pulse width. This means that range resolution increases from 150 m to 225 m. The range sampling was kept at 150 m (i.e, range oversampling was used) and thus there will be some range averaging but the 150 m sampling does offer greater resolution as compared to 225 m sampling. On the up side, use of a 1.5 μs pulse does increase the sensitivity of S-Pol. The new pulse shaper with a 1.5 μs pulse width was installed on 20 June. Since the fluctuating transmit powers in early June were monitored, this fluctuation will be calibrated out of the final S-Pol PRECIP quality controlled data set.

1.1 Operating Frequency and Antenna Patterns

The nominal operating frequency for S-Pol is 2809 MHz. Due to restrictions in Taiwan, the operating frequency was 2842.5 MHz. While no antenna patterns were cut at that frequency, RSF staff frequently scan the solar disk for pseudo patterns (Hubbert et al., 2010b). Such measurements suggest that the copolar pattern side lobes are somewhat larger (in power) at the $\pm 45^\circ$ cuts as compared to 2809 MHz. Sidelobe effects will be shown later. Figure 1 shows the V_{CO} - H_{CO} main lobe antenna pattern. The white circles show the 1° and 2° solid angles (the 1° solid angle marks the half power point). Just outside the 2° solid angle are regions of positive V - H power above and below the center while left and right of the center are regions of negative (dB) power. Since the pattern is V - H power, the above and

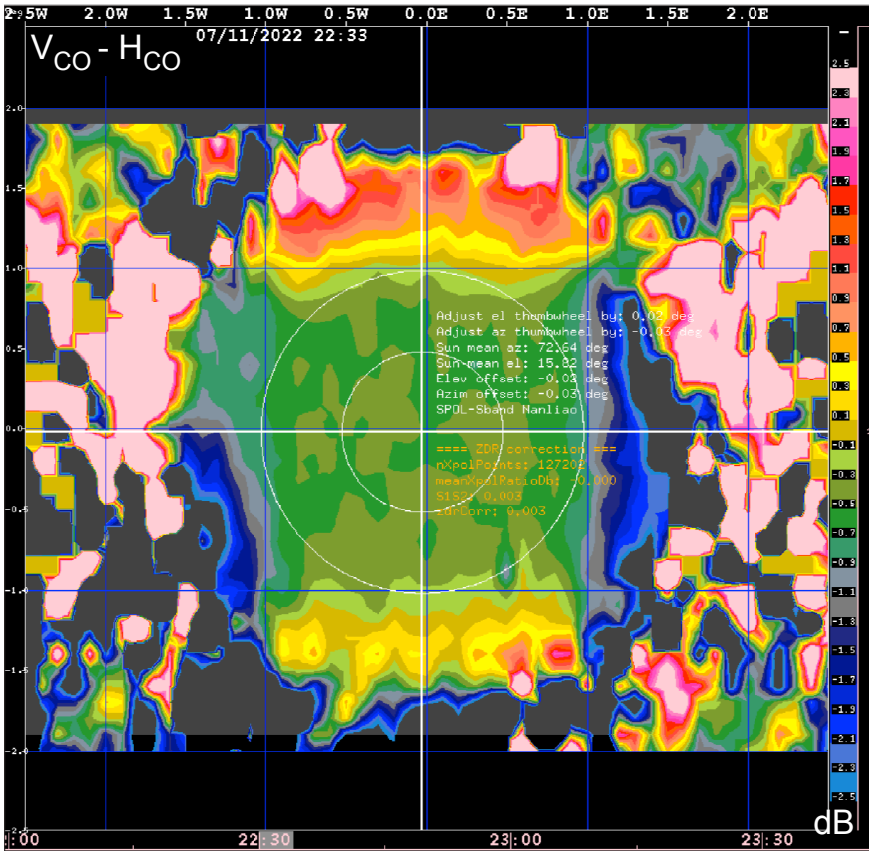

Figure 1: *The V - H pseudo antenna pattern obtained from a solar scan. The white circles designate the 1° and 2° solid angles. The S-Pol beam width is 0.93°. The red and yellow region above and below the beam center will bias Z_{DR} negative while the regions to the left and right of the center in blue will bias Z_{DR} positive. There is approximately a -0.5 dB offset in the center which is calibrated out of the measured Z_{DR}.*

below regions can cause negative Z_{DR} bias while the left and right regions can cause positive Z_{DR} bias. Examples of this are given below.

2 Clutter Environment

Figures 2 and 3 are pictures of the physical environment seen by S-Pol. Figure 2 shows a panorama (not including the ocean) of the S-Pol clutter environment taken from the pedestal of S-Pol. The center of the parabolic reflector is sum 10 feet higher. City buildings, vegetation and the mountains can be seen. On the left hand side of the panorama, the large building causing multi-path reflections is seen. Figure 3 shows a picture of the windfarm to the south west of S-Pol.



Figure 2: *A panorama view taken from the S-Pol pedestal showing the clutter environment of Taiwan island. Note the large building on the lefthand side which likely causes multi-path echoes as indicated in Fig. 4 (bottom image). Courtesy, Ben Crane.*



Figure 3: A picture of the windfarm to the south west of S-Pol.

The following S-Pol data plots are labeled in UTC. Sunrise is: ≈5:20 Local; 21:20 UTC. Sunset is: Local ≈18:30; 10:30 UTC.

Figures 4 to 7 demonstrate the radar clutter environment around S-Pol. There is no weather but some probable insect scatter is seen, evidenced by the high Z_{DR}s seen (red color scale). A thin white line marks the Taiwan coast line. Figure 4 shows the clutter reflectivity environment at 0.5°: top image is not filtered while the bottom image is clutter filtered data. From the northeast to the southwest there is considerable clutter first from Hsinchu and Zhubei and other buildings, then the mountains, and then the windfarm to the south-southwest. The bottom panel of Fig. 4 shows that the S-Pol clutter filter eliminates most of the clutter signal remarkable well. Likely due to the movement of the wind turbine blades, stronger echo residual from the windfarm is evident. To the north-northeast from S-Pol there is radial that is always contaminated by multi-path reflections from a nearby (to S-Pol) building (see Fig. 2 at the top left).

Also marked to the near west of S-Pol, in Fig. 4 bottom, is a region of sea clutter. The center

of S-Pol's parabolic reflector is approximately 10.6 m high and using an approximation formula for the ocean horizon: sqrt[hight of antenna X 13] yields 11.7 km horizon range, which is shown on Fig. 4 on the bottom panel. Since the propagation wave of the radar beam in a standard atmosphere is bent towards earth according to the "4/3 earth curvature rule", the radar horizon is extended a bit beyond the 11.7 km to about 13.5 km.

Figure 5 is similar to Fig. 4 but for 4° elevation angle. Even though the center of the main radar beam is above all the clutter, the side lobes (and part of the main beam) of the antenna pattern still see the clutter targets. However, as the bottom panel shows, the clutter filter eliminates the very large majority of the clutter signal. Also note in the top unfiltered reflectivity panel, streaks of constant radius reflectivity. These are also due to side lobes picking up strong reflectivity targets.

Figure 6 shows the Z_{DR} corresponding to Figs. 4 and 5 for 0.5° (top) and 4° (bottom) elevation angles. The top panels shows that the sea clutter is primarily blue color scale indicating negative Z_{DR}. The horizontally polarized wave has a propensity to glance off from the surface and continue on away from the radar whereas the vertically polarized wave is more likely to reflect back to the radar thus making Z_{DR} negative (see Long (2001)). Other negative Z_{DR} regions are more difficult to explain but outside the 25 km range ring the SNRs are quite low. Under atmospheric super refraction conditions, the radar bean will be bent toward the earth (i.e., AP clutter) and thus sea clutter can be seen further out from the radar. An example will be given later.

Figures 7 shows the filtered velocity field for 0.5° (top) and 4° (bottom) elevations. Where there is coherent velocity structure, biological scatter is indicated (from high Z_{DR}). The area just to the east of the S-Pol at 0.5° elevation has an odd velocity structure and this could be due to multi-path reflections from buildings.

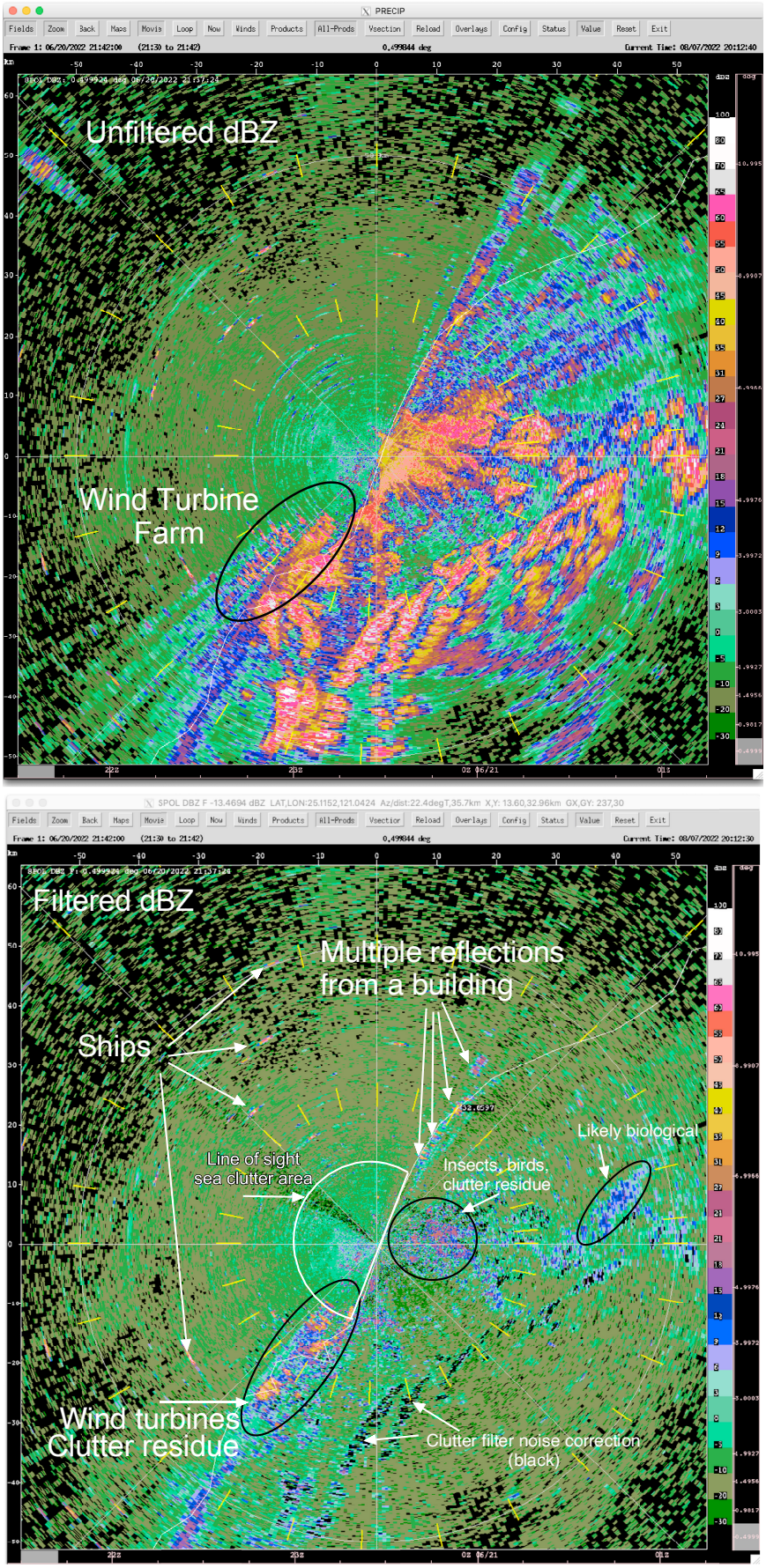

Figure 4: Clutter environment. Top dBZ not filtered, bottom, dBZ filtered. Elevation 0.5°. The thin white line outline Taiwan.

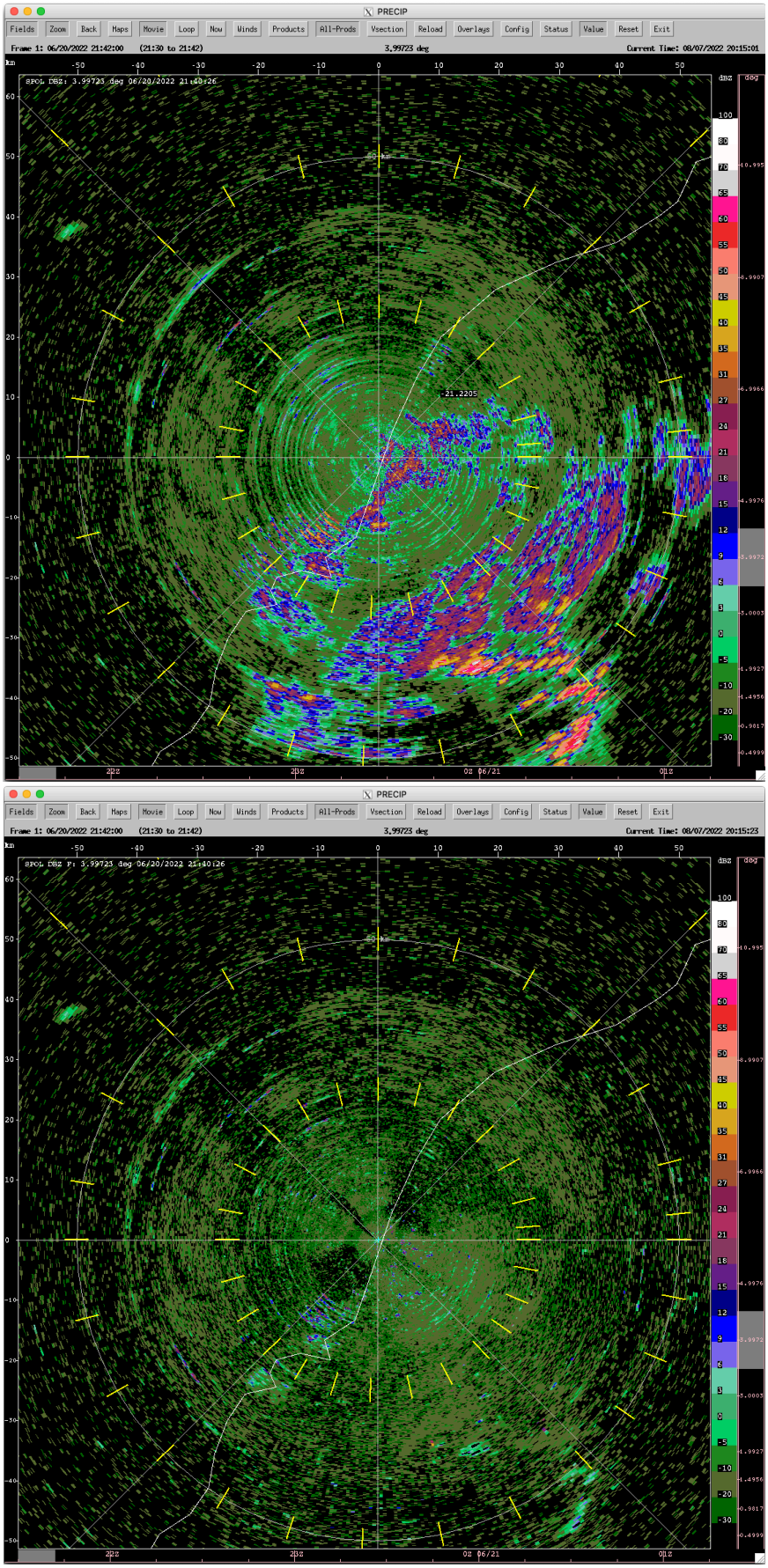

Figure 5: Clutter environment. Top dBZ not filtered, bottom, dBZ filtered. Elevation 4°. The thin white line outline Taiwan.

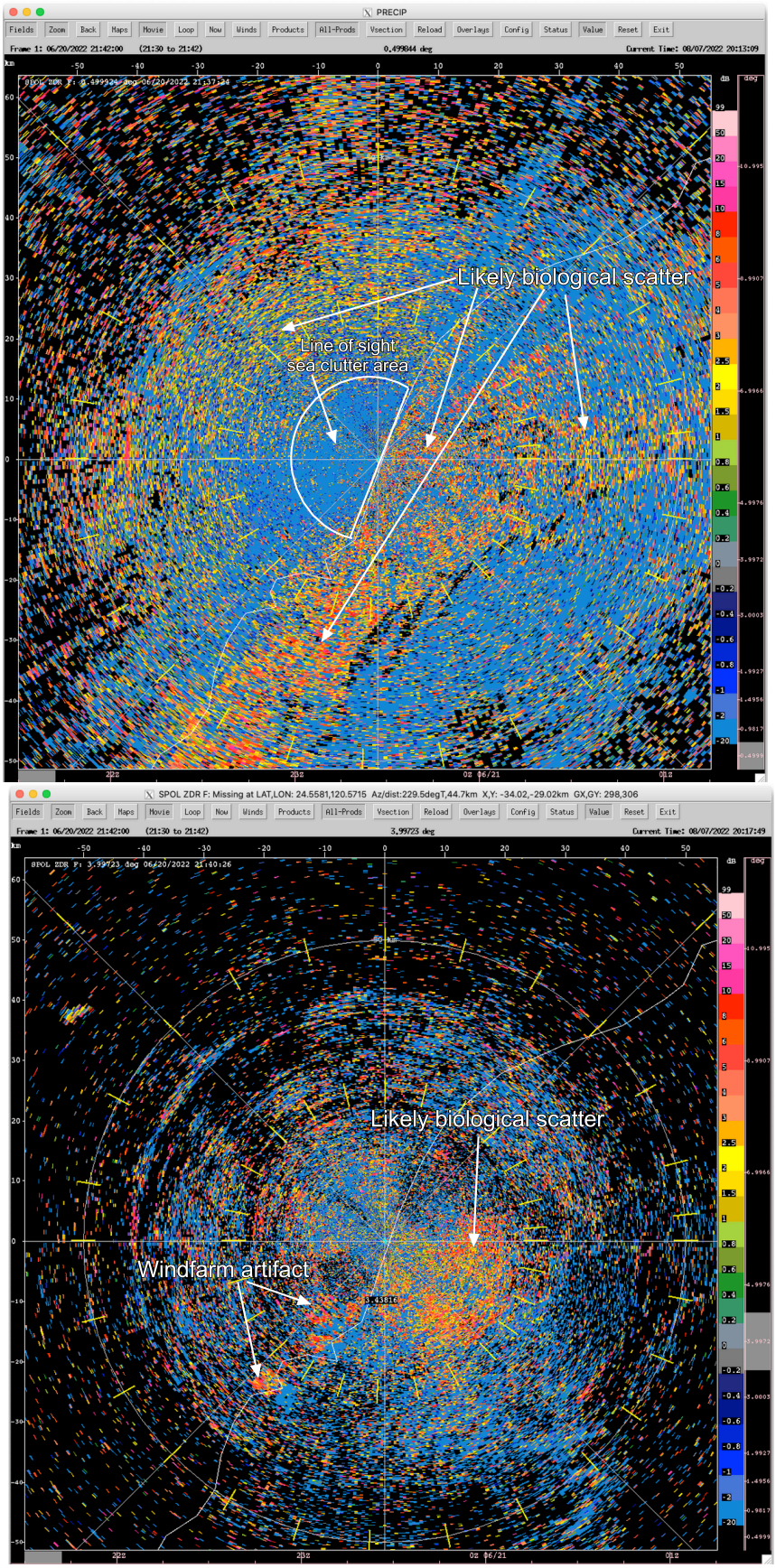

Figure 6: Clutter environment. Top Z_{DR} not filtered, bottom, Z_{DR} filtered. Elevation 4°. The thin white lines outline Taiwan.

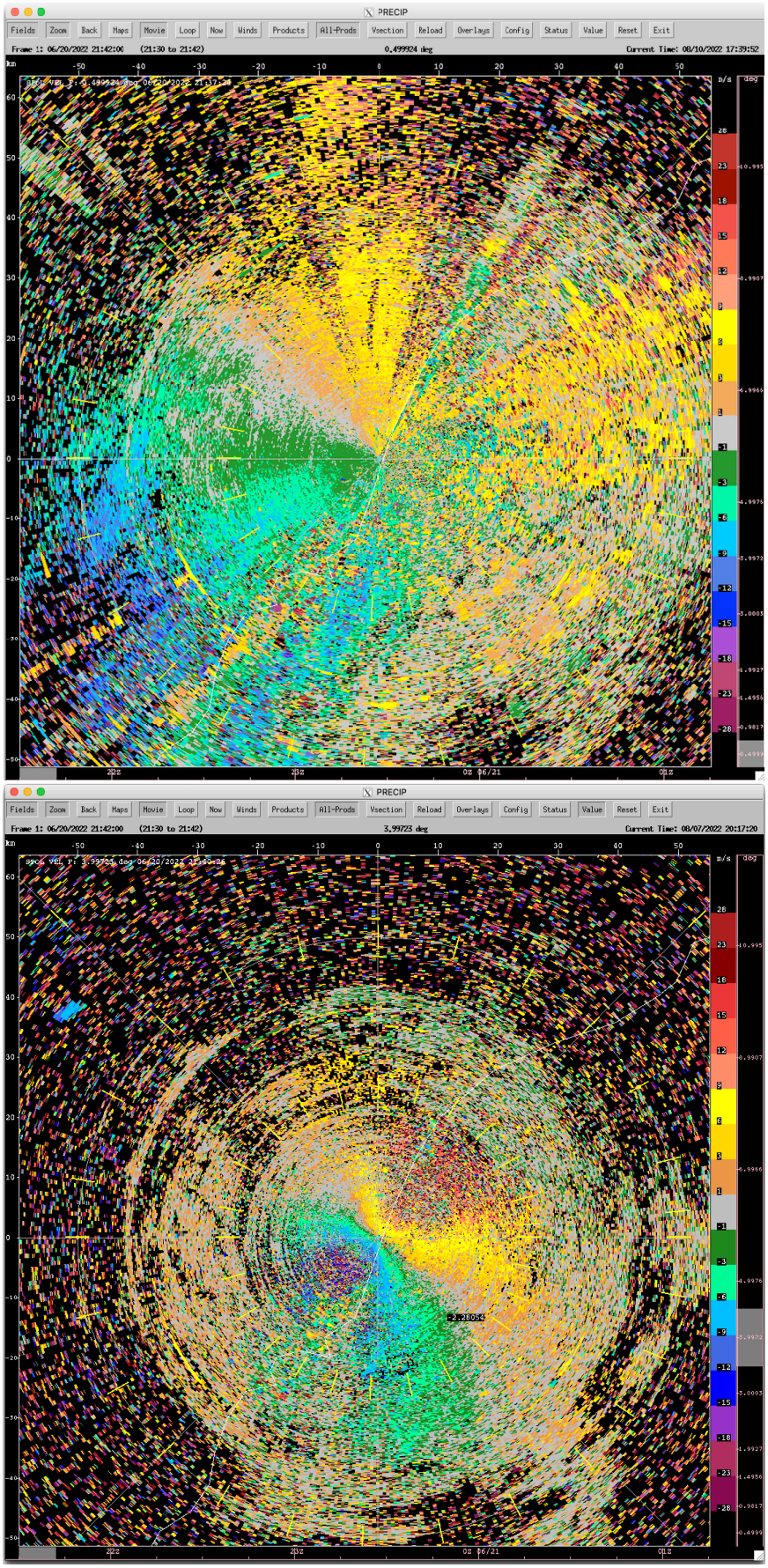

Figure 7: Clutter environment, filtered velocity. Top , 0.5°, bottom 4° elevation. The thin white line outline Taiwan.

3 RHIs of a Large Convective Cell

Figures 8 and 9 show a very tall convective cell with reflectivities higher than 31 dBZ above 18 km agl. Figure 8 shows reflectivity (top) and velocity (bottom). A classic velocity cut with convergence below 9 km and divergence above 9 km agl is seen. Figure 8 shows Z_{DR} (top) and K_{DP} (bottom). Radial Z_{DR} streaks are seen in the ice phase. These are caused by ice crystals that are canted due to charge separation (i.e., electrification). The canted ice crystals cause H to V cross coupling as the wave propagates through the storm. See Hubbert et al. (2018, 2015, 2010b,a, 2014a,b) for discussions of H-to-V cross coupling and how that affects polarimetric signatures.

4 Meiyu Front and Multi-path Reflections

The first part of PRECIP 2022 focused on capturing precipitation due to the Meiyu Front. Several fronts did come out of China, across the Taiwan strait and strike Taiwan. Because of the wide spread nature of the fronts, they gave rise to easily observed multi-path reflections off the buildings of the Hsinchu area. Figure 10 shows one PPI example with reflectivity (top) and velocity (bottom). The elevation angle is 0.5°. This figure exemplifies the anomalous multi-path scattering cause by the buildings to the east of S-Pol which are visible in the panorama of Fig. 2. The many radial streaks caused by the buildings are easily seen in the velocity image of Fig. 10. Look closely along the radial steaks on the velocity plot of Fig. 10 bottom. For example look along the radial streak at about 30° azimuth and flow that radial 180°s out along the $30 + 180 = 210°$ radial. The velocities along the 210° are similar to the velocities along the 30° radial. This is also true for the radial streak at about 178° azimuth. This suggests the following path of the radar beam. The transmitted pulse reflects off from the building back at the radar. The wave then continues to propagate in the direction opposite of the transmitted direction where some of it is scattered by the precipitation particles. The building can be thought of as a large sub-reflector of the radar transmitted radar beam. The wave scattered by the precipitation particles travels back to the building where it is again reflected back at the radar antenna where it is received with the velocity signature of the precipitation particles. The building may not be perpendicular to the line of sight of the radar and the wave is reflected in some other direction. However, the precipitation particles can still

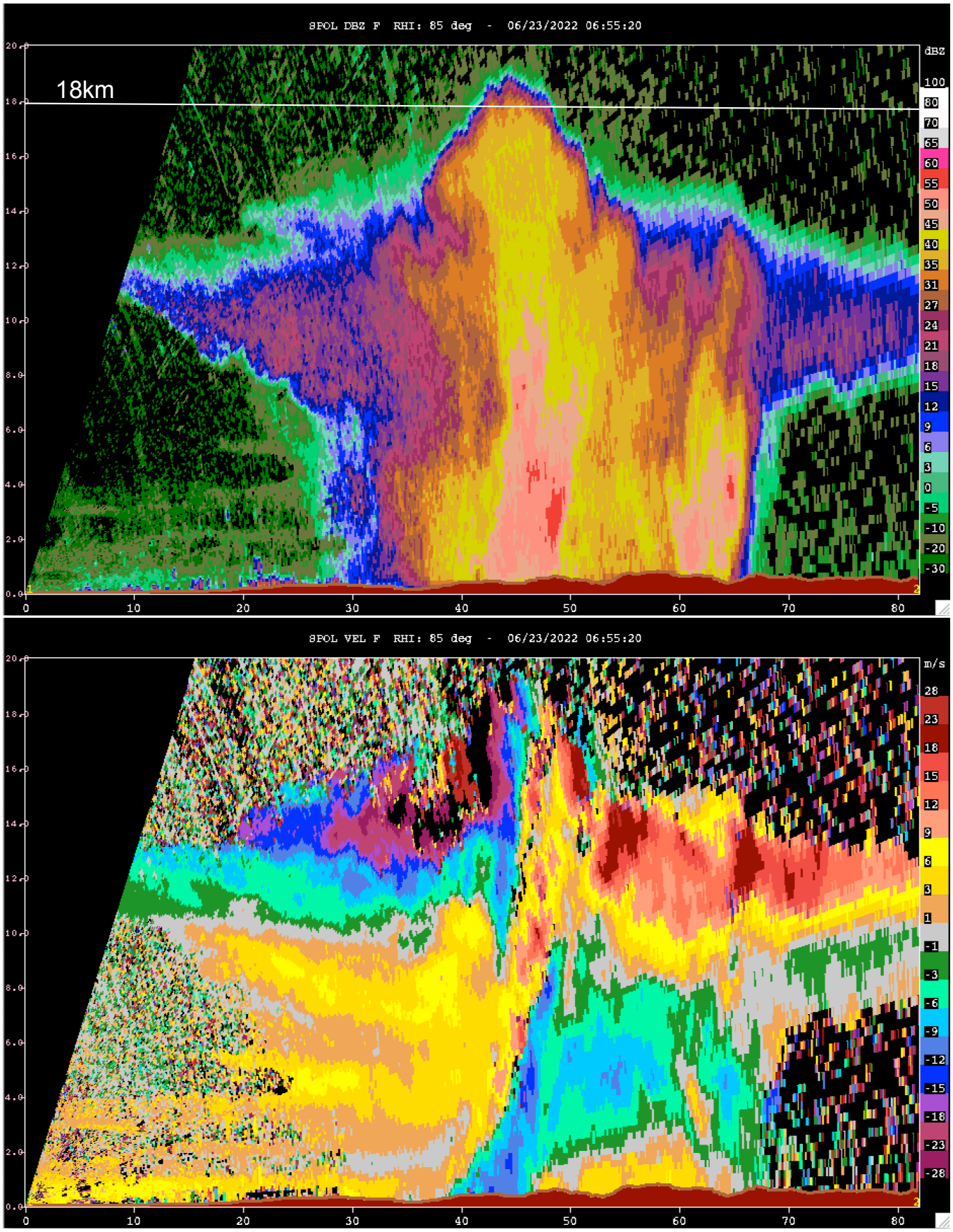

Figure 8: Large convective cell. Top reflectivity, filtered; bottom, Velocity filtered. Over 31 dBZ above 18km.

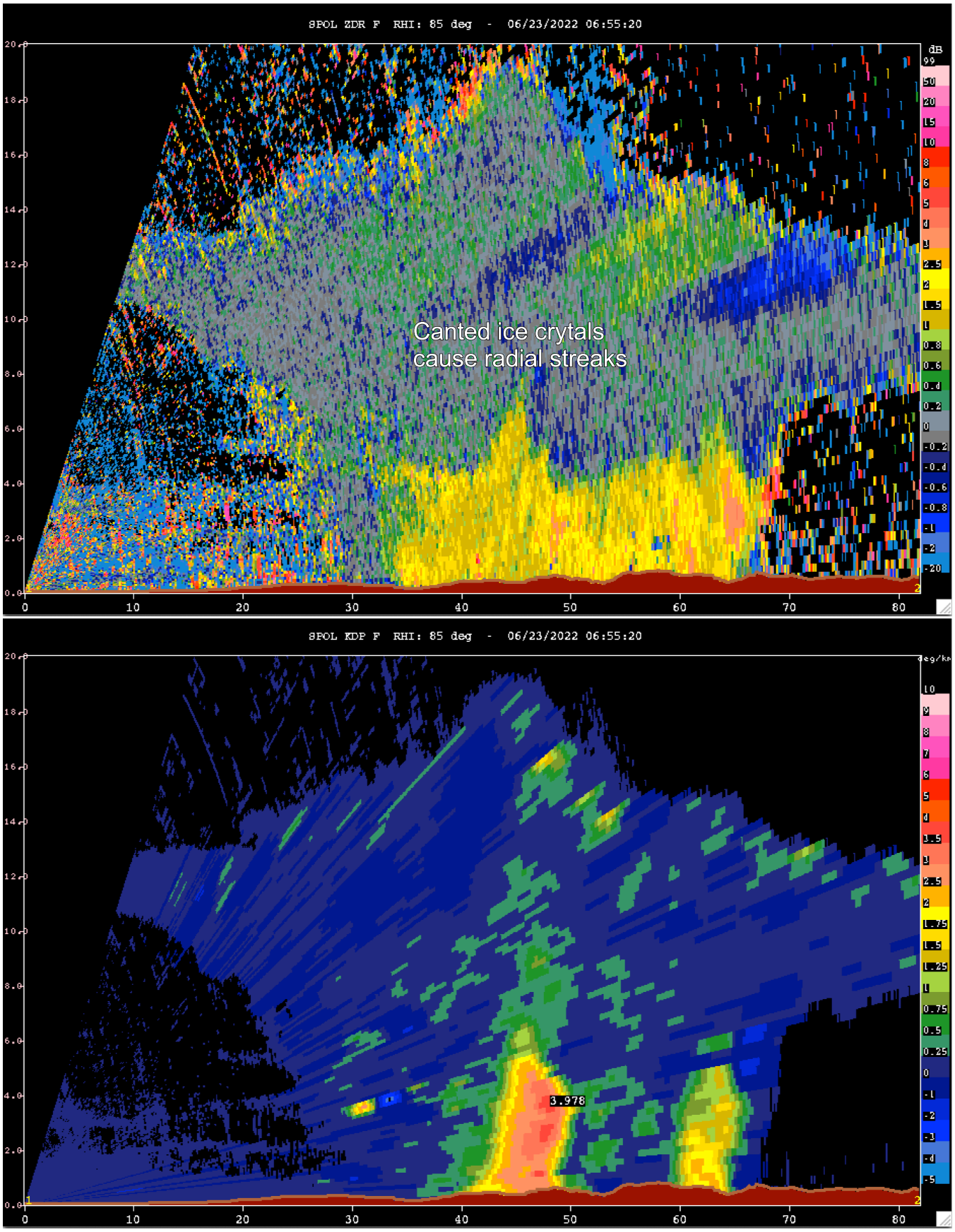

Figure 9: Large convective cell. Top Z_{DR}, filtered; bottom, Velocity K_{DP} filtered. Over 31 dBZ above 18 km. A K_{DP} of 4° km^{-1} corresponds to about 140 mm h^{-1} depending on the formula used.

reflect energy back at the building which will return it to the radar. In this way, other velocities can be detected by the radar other than those along the 180° line, provided there is enough SNR. These streaks are particularly evident when a long, wide spread line of precipitation approaches from the west, leaving clear air to the east, of S-Pol such as a Meiyu Front. Fortunately, the large majority of these streaks are characterized by low ρ_{HV} values and can thereby by eliminated by using a ρ_{HV} threshold.

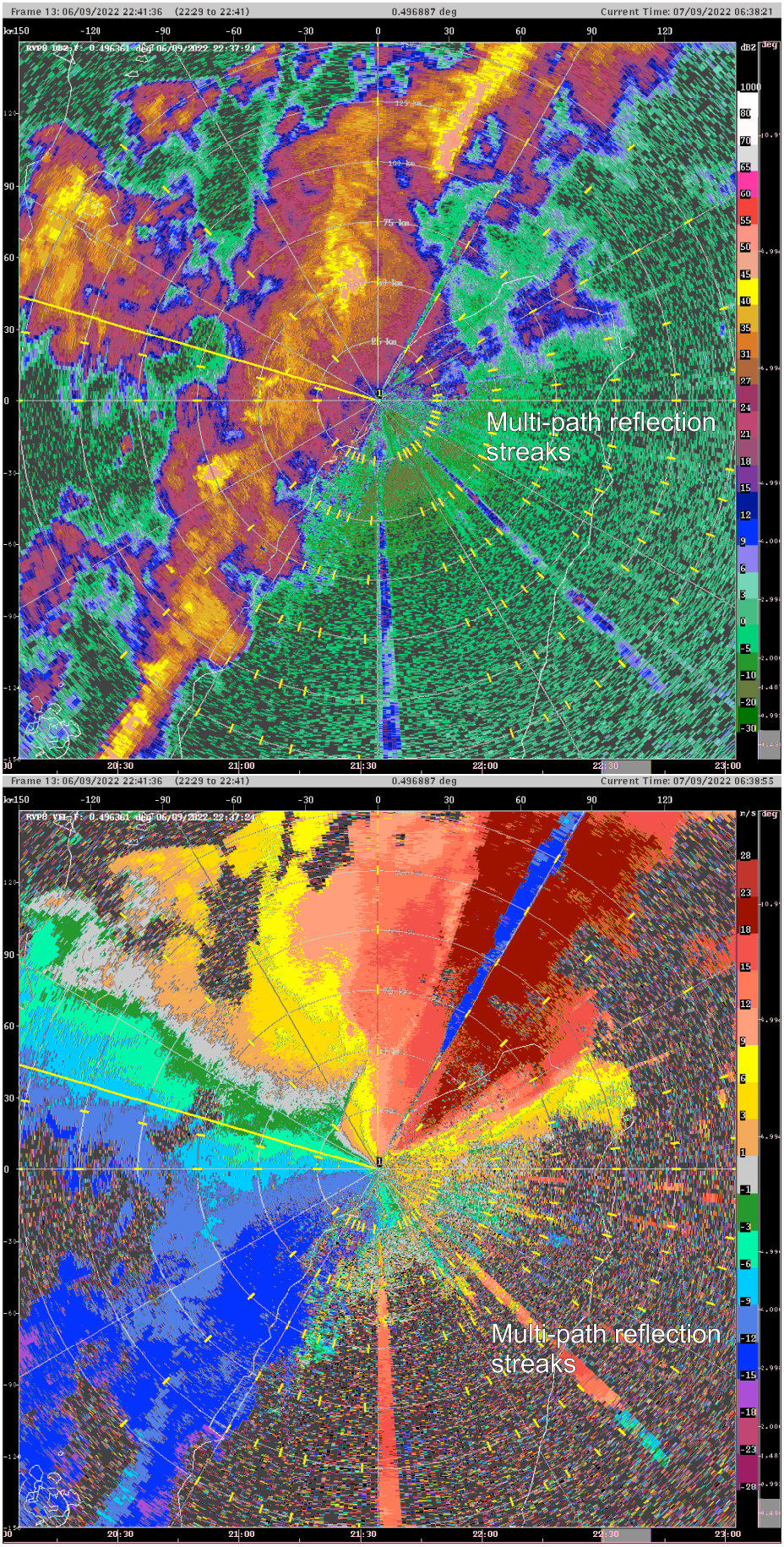

Figure 10: MeiYu front and Multi-path Reflections. Top reflectivity, bottom velocity. The thin white lines outline Taiwan.

5 Chaff Polarimetric Signatures

Chaff releases occurred several times a week in the observation area of S-Pol during PRECIP. These releases are likely related to the conflict between Taiwan and China and are related to radar jamming. In any event, there are many S-Pol observations of chaff during PRECIP, which was a new experience for S-Pol. Figure 11 shows a picture of chaff taken from Kurdzo et al. (2018). The fibers are quite thin and light and are metallic-coated silica fibers which are highly reflective.

Figures 12 to **??** document the radar signature of chaff. Much more detail about chaff radar signature is found in the paper by Kurdzo et al. (2018). S-Pol does scan much more slowly than the WSR-88Ds and thus the following images are of high data quality.

The caff in this case was released around 4:40UTC on 3 July at approximately 50 km range at 350° azimuth and then drifted toward Taiwan. The chaff remained visible over northern Taiwan until after 15UTC. Figure 12 shows the reflectivity (top) and the velocity (bottom) at 9:39UTC at 3° elevation as it moved over Taiwan. The reflectivity and velocity do resemble a possible precipitation cloud. Figure 13 shows the accompanying spectrum width (top) and ϕ_{DP} (bottom). The spectrum widths are quite narrow but could be indicative of precipitation particles. ϕ_{DP} however appears random and indicates little correlation between the H and V channels, uncharacteristic of precipitation. Figure 14 shows a rather bizarre Z_{DR} field (top) while the bottom image is ρ_{HV} which shows very low correlation in the chaff region as expected. The negative Z_{DR}s go below -10 dB and the positive Z_{DR}s go above 10 dB. Figure **??** shows an RHI through the chaff of reflectivity (top) and Z_{DR} (bottom) at 9:47UTC. The Z_{DR} demonstrates an interesting layering effect with high Z_{DR} on top of the negative Z_{DR} layer. Such a signature is apparently common (Kurdzo et al., 2018). One explanation offered is that the some of chaff vertically aligns itself and therefore falls faster than the chaff that remains more horizontally aligned. Fair weather electric field calculations are done in (Kurdzo et al., 2018) and indicate that the electric field could indeed align the chaff vertically. Other explanations are offered in (Kurdzo et al., 2018). In any event, the extremely high and low Z_{DR} values are one distinguishing feature of chaff. Fortunately again the ρ_{HV} is low in chaff and can be used as a threshold to eliminate a large majority of the chaff contamination.



Figure 11: A picture of chaff. Taken from Kurdzo et al. 2018, Polarimetric Observations of Chaff Using the WSR-88D Network, JAMC.

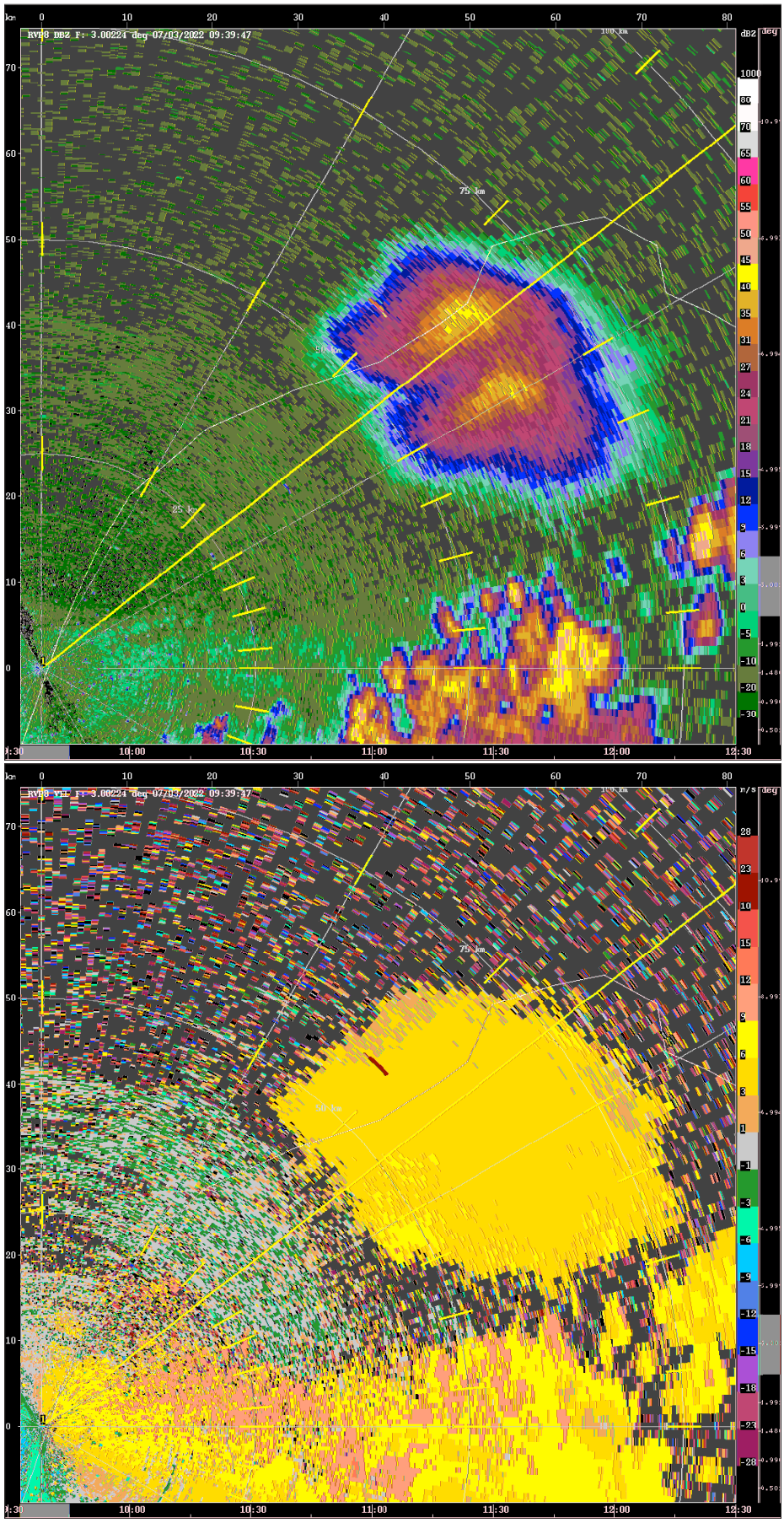

Figure 12: Reflectivity (top) and velocity (bottom) from a chaff cloud on 3 July at 0939UTC.

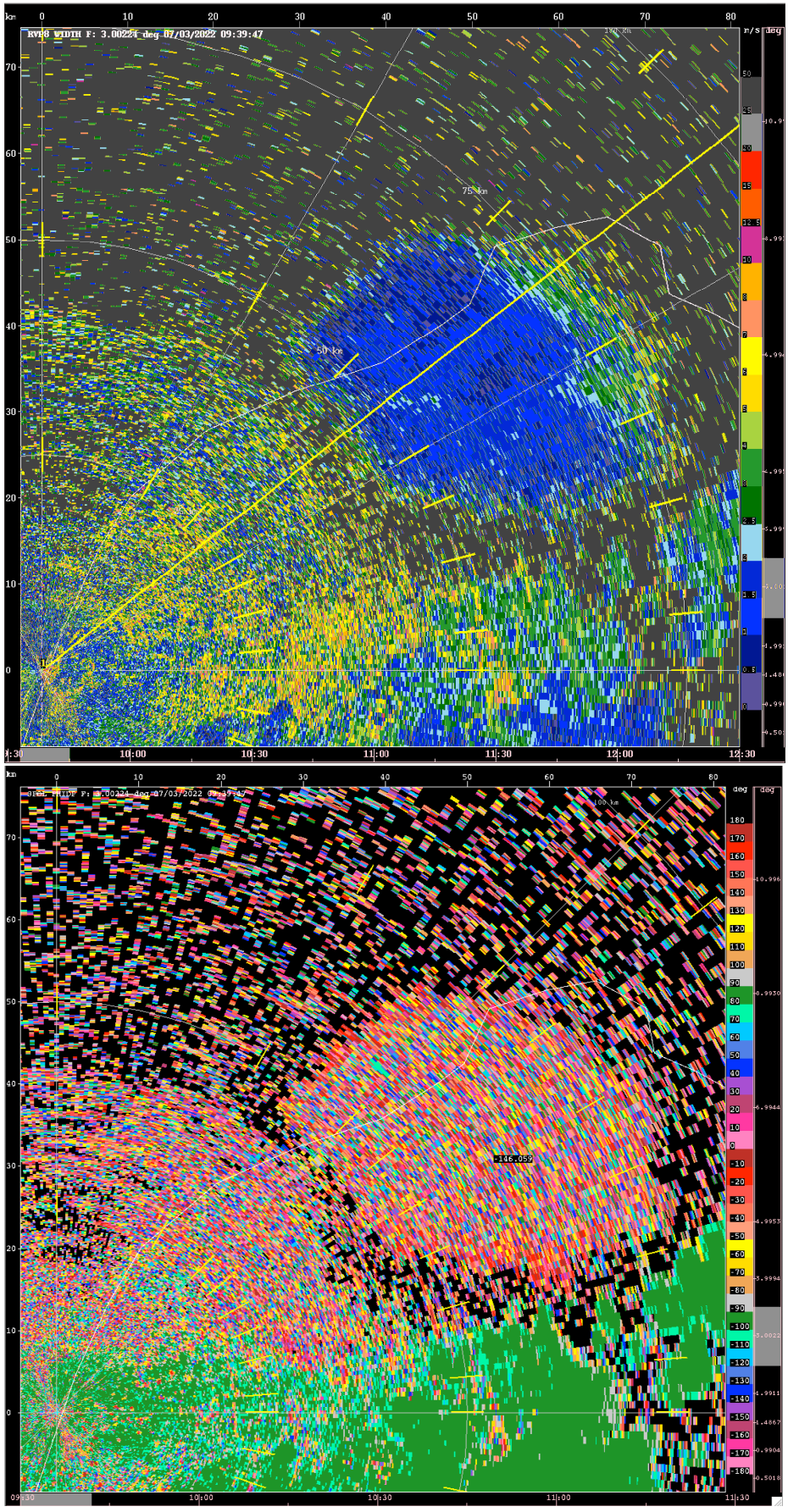

Figure 13: Spectrum width (top) and ϕ_{DP} (bottom) corresponding to Fig. 12. The thin white line outlines Taiwan.

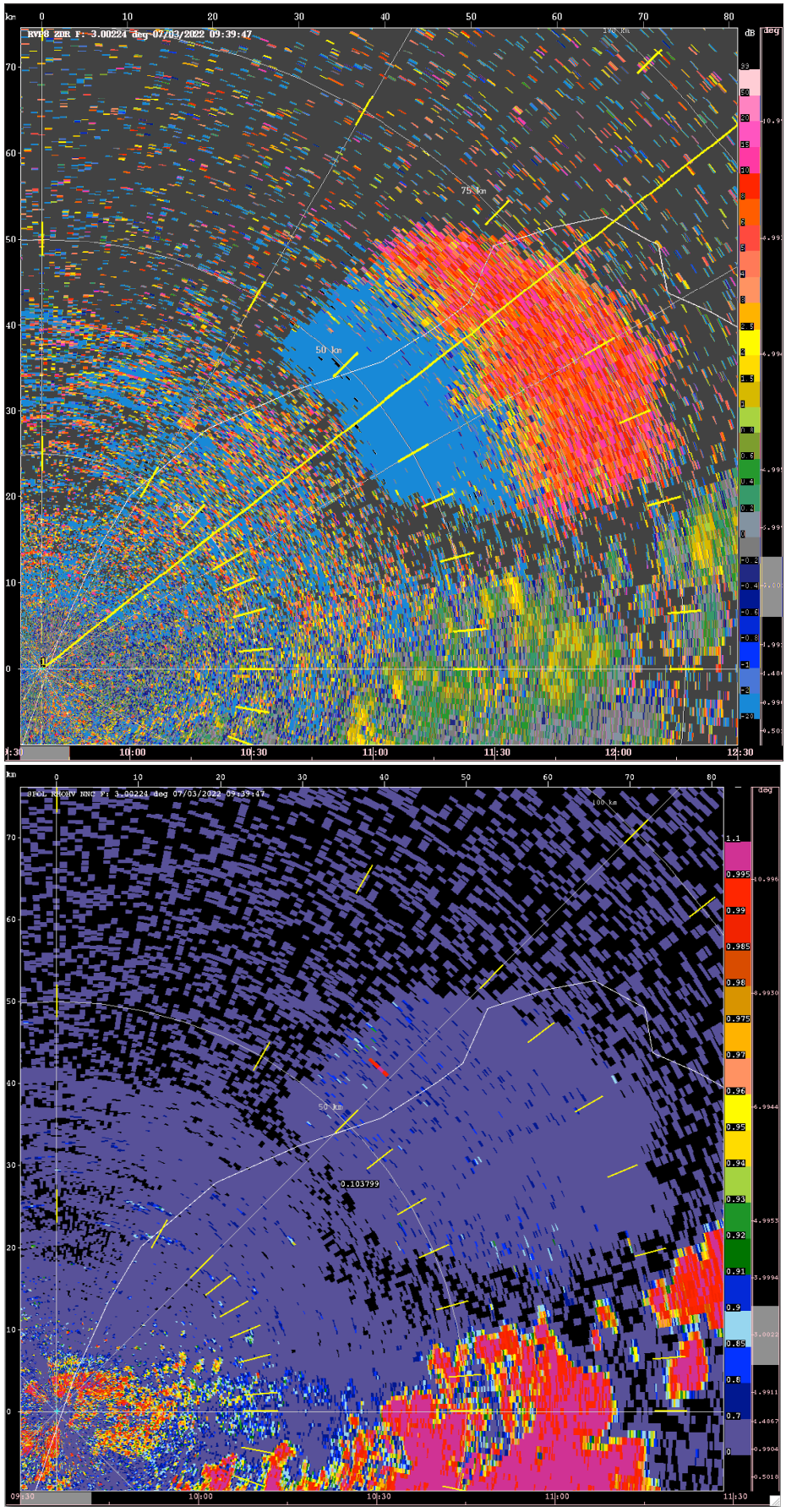

Figure 14: Z_{DR} (top) and ρ_{HV} (bottom) corresponding to Fig. 12. The thin white line outlines Taiwan.

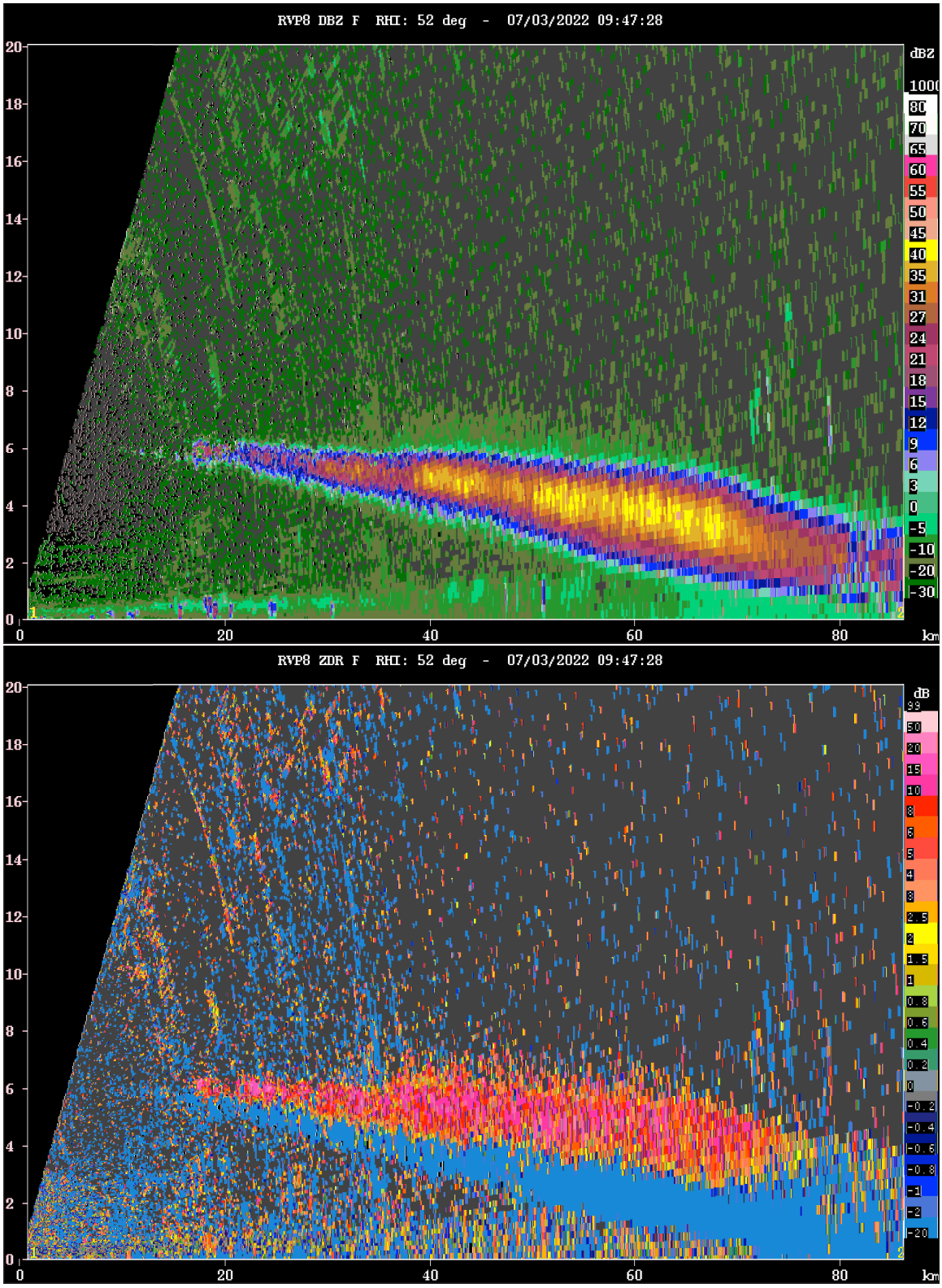

Figure 15: An RHI of reflectivity (top) and Z_{DR} (bottom) through a chaff cloud on 3 July at 0947UTC. Presumably the fair weather electric field aligns some of the chaff particles which then descend faster than the other horizontally aligned chaff thereby causing negative Z_{DR} on the bottom.

6 Scatter from Ships in the Taiwan Strait

There is much sea vessel traffic in the Taiwan strait and naturally, when the ships come into the line of sight of S-Pol, S-Pol will "see" them. Some of the vessels are container ships with very large, flat metal surfaces which will efficiently reflect microwaves. The direction of the reflected microwaves depends on the ships' orientation to S-Pol. The reflected microwaves can return toward Taiwan where there are also many buildings, other man made objects, insects and weather that can reflect the microwaves back at the ships where they are once again reflected back toward S-Pol. Such multi-path signals will manifest themselves in back of the ship along the ship's radial. Figure 16 shows an example of such a ship scattering case. The top image is reflectivity while the bottom image is maximum reflectivity in a column. The 300° radial shows a reflectivity streak in back of a ship marked by a red arrow in the top panel. Other ships are also indicated. In the bottom image (max. dBZ in a column), the ships appear to have grown wings along each side of the ship. These are due to sidelobes. As S-Pol scans on either side of the ship at higher elevation angles, sidelobes see the ship. S-Pol sidelobes at $\pm 45^{\circ}$ are the highest due the 4-support strut topology of the S-Pol antenna. Movie loops of max. dBZ are a good way to view the ships movement. Figure 17 show a screen dump of a webpage that tracks the movement of ships in the Taiwan strait: www.marinevesseltraffic.com/TAIWAN-STRAIT/ship-traffic-tracker.

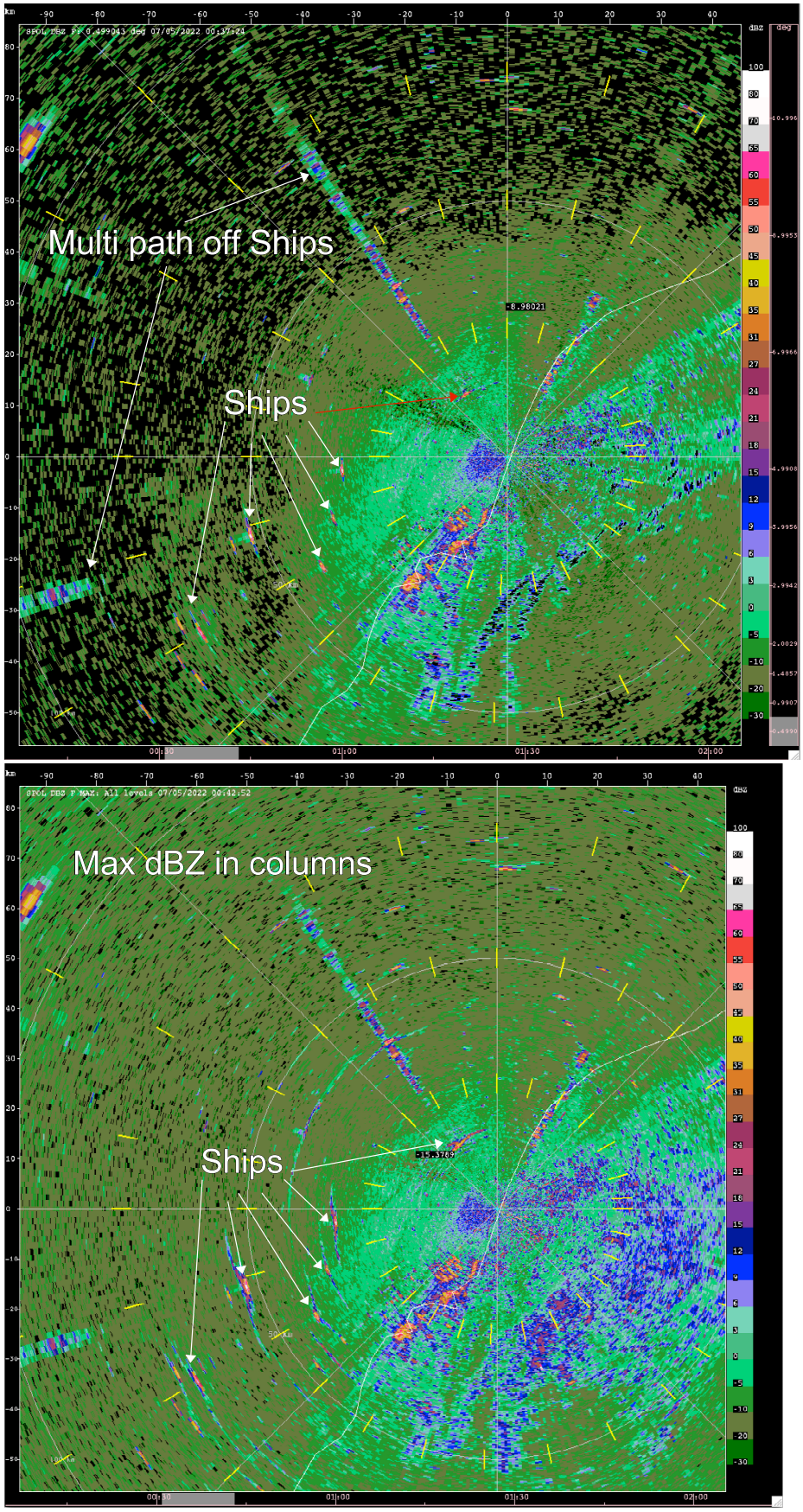

Figure 16: An example of scatter off ships in Taiwan strait. Top reflectivity filtered; bottom, maximum dBZ in a column. Multi path reflection are evident from the streaks along te ships's radial. The ships look like have "wings" in the max. dBZ plots on the bottom. These are due to sidelobes.

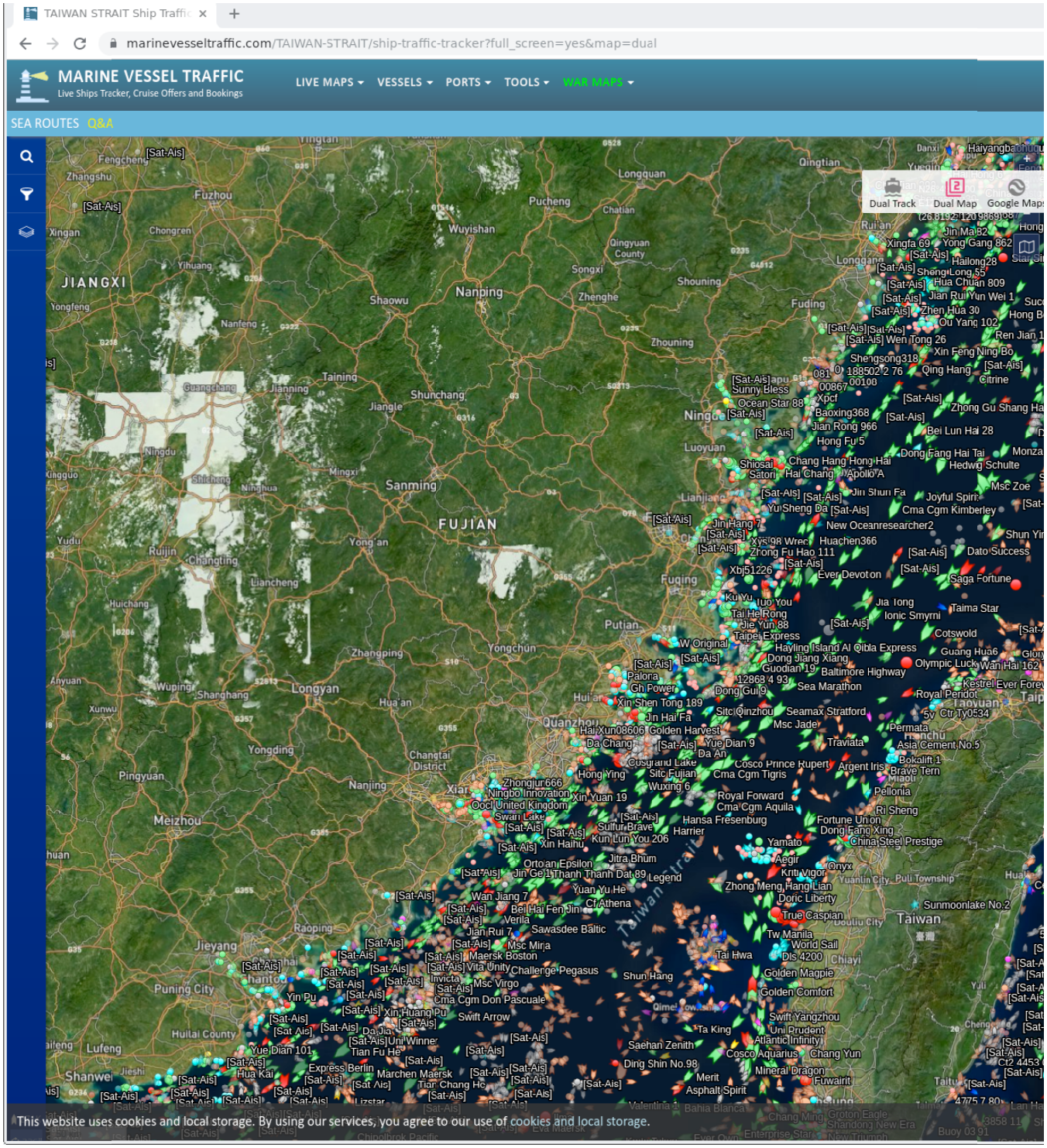

Figure 17: A screen dump from the webpage https://www.marinevesseltraffic.com/TAIWAN-STRAIT/ship-traffic-tracker. This webpage tracks vessels in the Taiwan Strait in real time.

7 Anomalous Propagation (AP) Clutter

Anomalous propagation (AP) clutter was frequently observed to the west and north west of S-Pol. Figures 18 to 20 give an example of this. Figure 18 shows unfiltered reflectivity from a non AP day 8 July (top) and from an AP day, 9 July (bottom). The elevation angle is 0.5°. The thin white line on the left hand side of the images is the coastline of China. Figure 19 shows unfiltered velocity (top) and filtered reflectivity (bottom) corresponding Fig. 18 bottom. Most of the clutter over land has been eliminated by the filter. There is remaining echo over the ocean. Figure 20 shows Z_{DR} filtered top and ρ_{HV} filtered (bottom). The negative Z_{DR} and the very low ρ_{HV} indicate that the remaining signals are not weather and thus is AP clutter from the sea surface. In the ρ_{HV} plot, there are many red streaks with a constant radius. These are very likely due to ships.

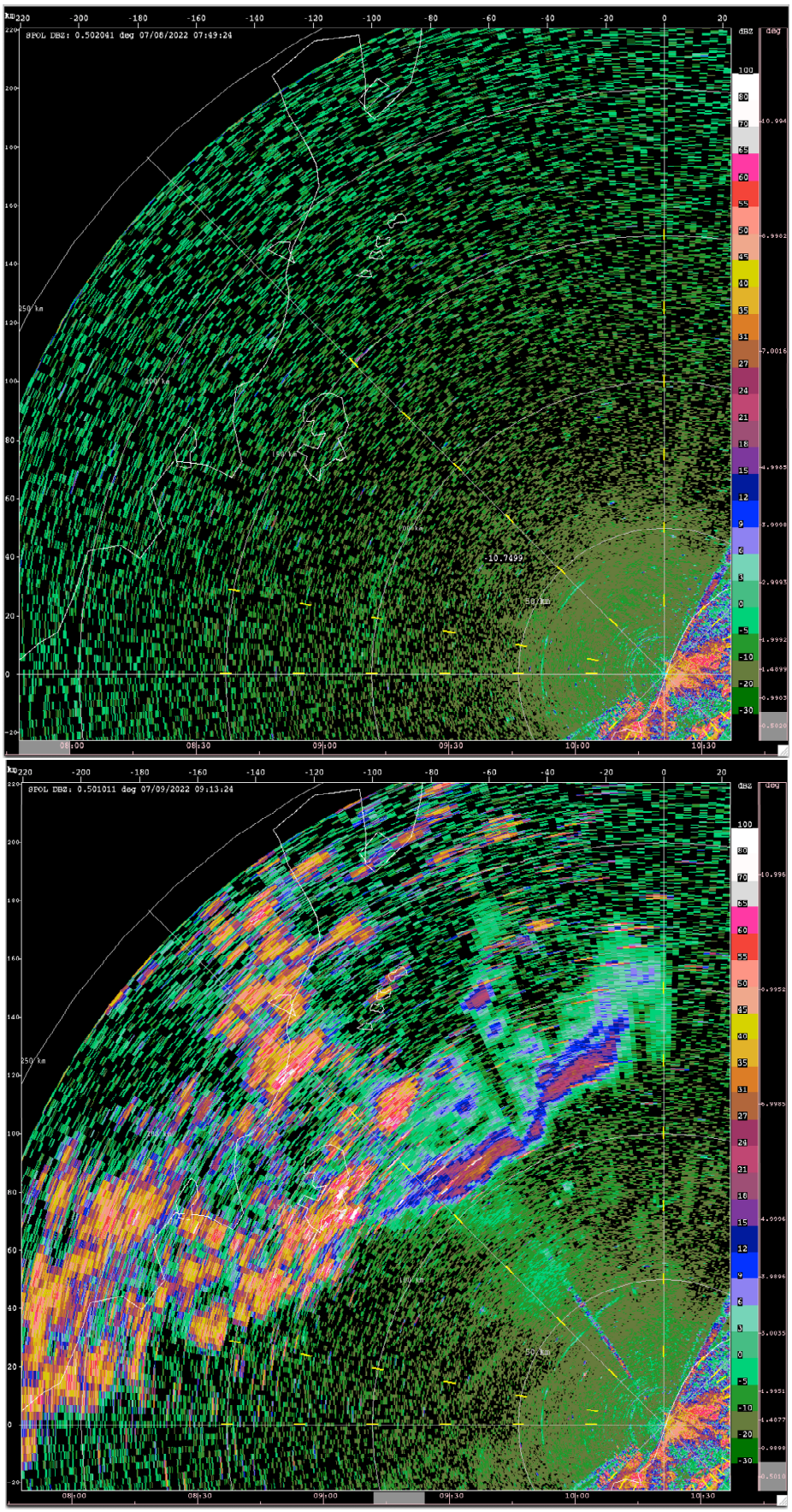

Figure 18: AP clutter example. Top: reflectivity on a non AP day, 8 July at 7:49UTC. Bottom: AP clutter reflectivity on 9 July at 9:13 UTC. 0.5° elevation for both images.

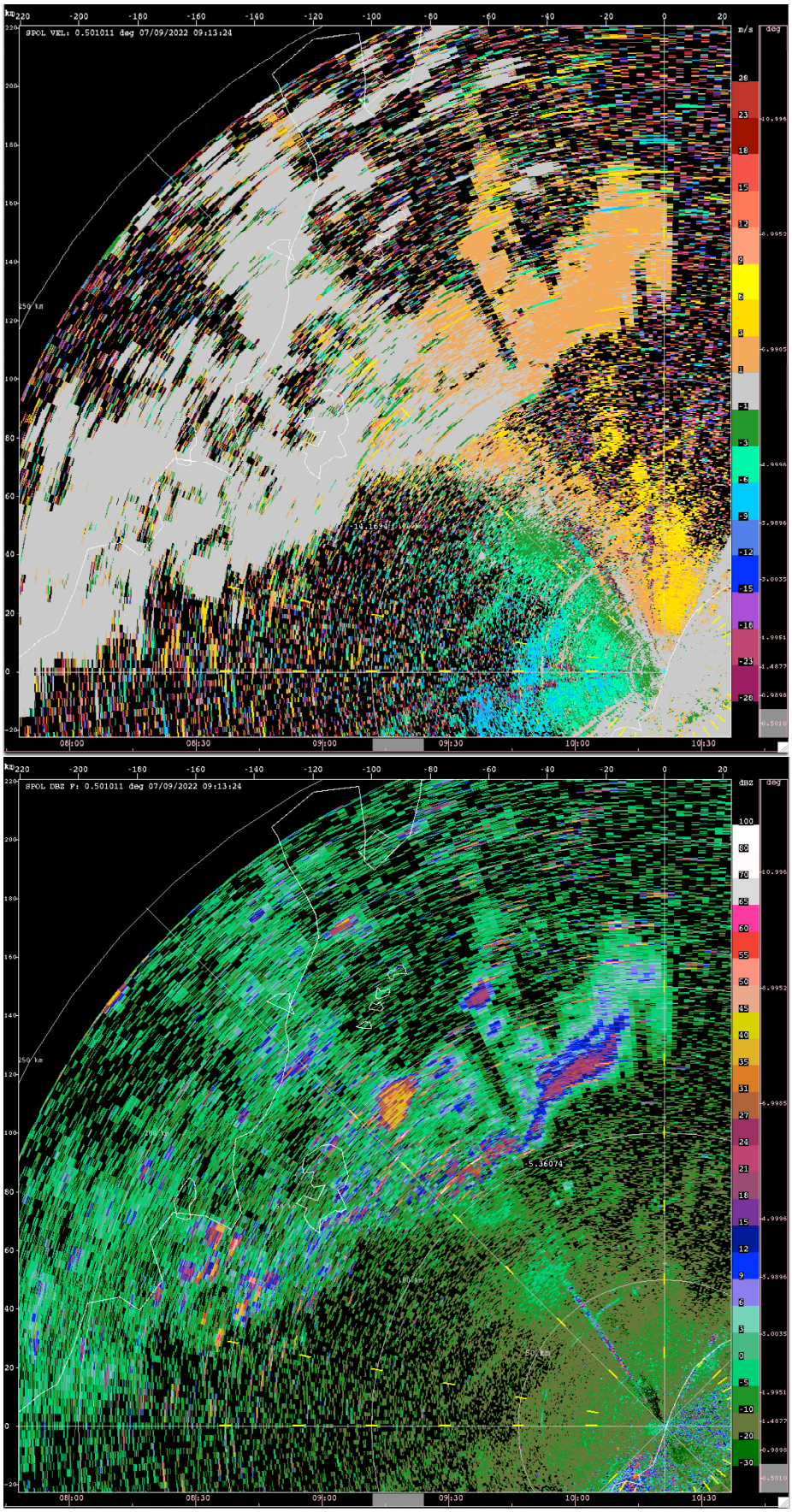

Figure 19: AP clutter plots corresponding to Fig. 18 bottom. Top: velocity unfiltered. Bottom: reflectivity filtered.

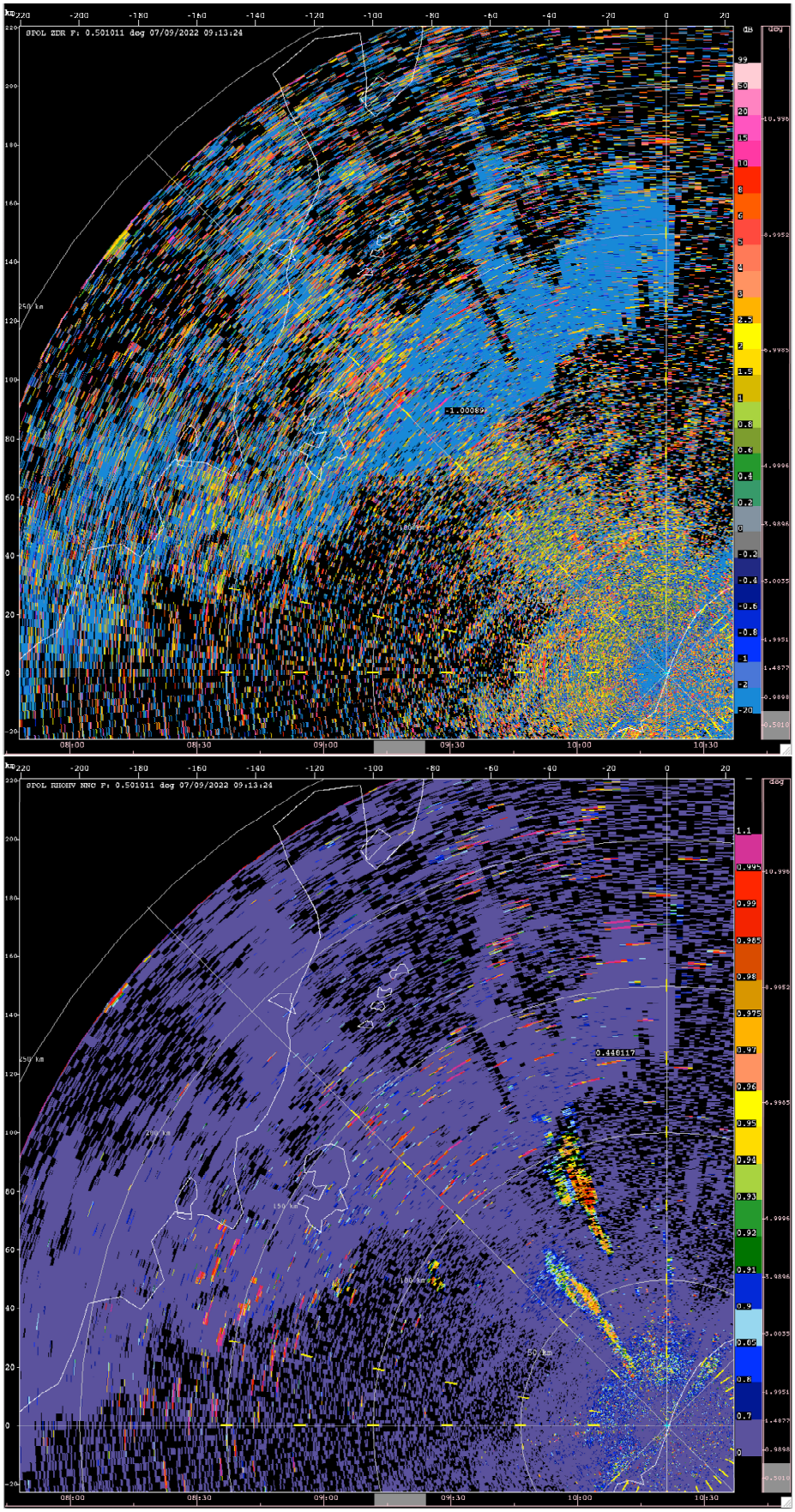

Figure 20: AP clutter plots corresponding to Fig. 18 bottom. Top: Z_{DR} filtered. Bottom: ρ_{HV} filtered without noise correction.

8 Insect Scatter and Behavior in Taiwan

During the warmer months (temperatures $> 10°$C) insects typically fill the skies over almost all land areas of the world. The literature contains numerous articles of such observations (Mueller and Larken, 1985; Wilson et al., 1994; Melnikov et al., 2015; Zrnić and Ryzhkov, 1998; Chilson et al., 2012; Vivekanandan et al., 2013; Lang et al., 2004; Drake and Reynolds, 2012). In a recent study in the United Kingdom (UK), researchers estimate that over the southern UK for high-flying (> 150 m) insects, "that about 3.5 trillion insects (3200 tons of biomass) migrate above the region annually" (Hu et al., 2016). Thus, insects are everywhere including Taiwan.

Many times thin lines of reflectivity with corresponding high Z_{DR} are produced by Gust Fronts that consolidate insects. This was not seen in Taiwan or perhaps we missed it. In many locations, such as PECAN, insects are observed migrating in a particular direction and thus cause the classic hour glass shape reflectivity signature. This was also not observed but the insects in Taiwan at this time of year appear to have random individual flight patterns. We did observe that many insects in Taiwan come out at night. This is demonstrated in the following plots with one set of plots before sunset with the other set just after sunset.

Figure 21 shows reflectivity at 1.5° elevation angle. The top is before sunset and the bottom is after sunset. One can see an increase in reflectivity close to the radar. Figure 22 shows the accompanying Z_{DR} again before sunset on top and after sunset on bottom. The increase in high Z_{DR} values (red color scale) is clearly seen. This is a classic signature of many insects with elongated bodies. The insects are demarked by the land boundary of Taiwan but later into the night, insects are seen in increased number over the ocean too. Figures 23 and 24 are similar format to Figs. 21 and 22 but in RHI format. The yellow radial line in the PPI plots marks the RHI azimuth. Figure 24 bottom shows the increase in the red Z_{DR} region after sunset. Insects were observed at higher altitudes later into the night.

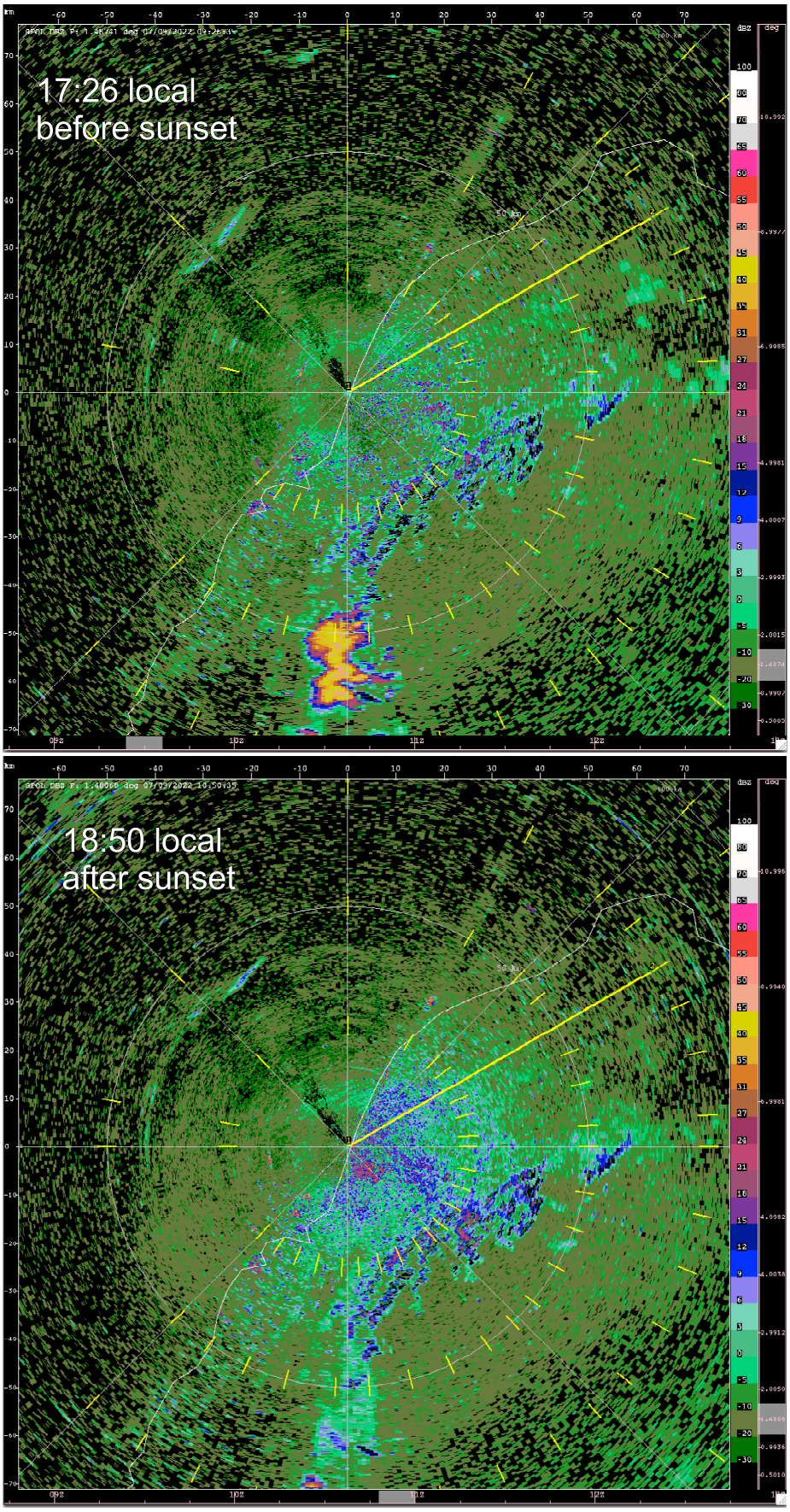

Figure 21: Insect reflectivity, filtered. Top: before sunset. Bottom: after sunset.

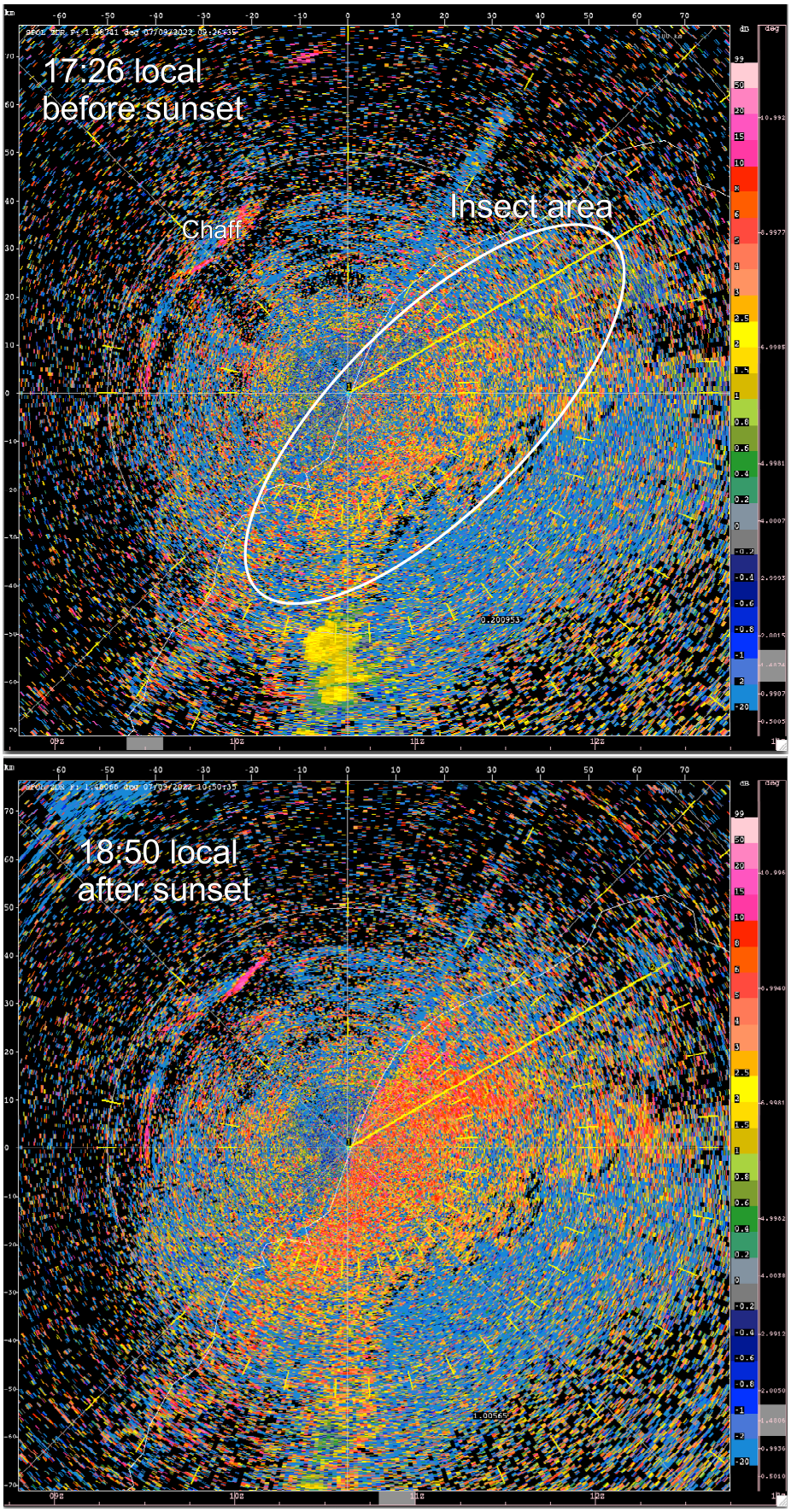

Figure 22: Insect Z_{DR}, filtered. Top: before sunset. Bottom: after sunset.

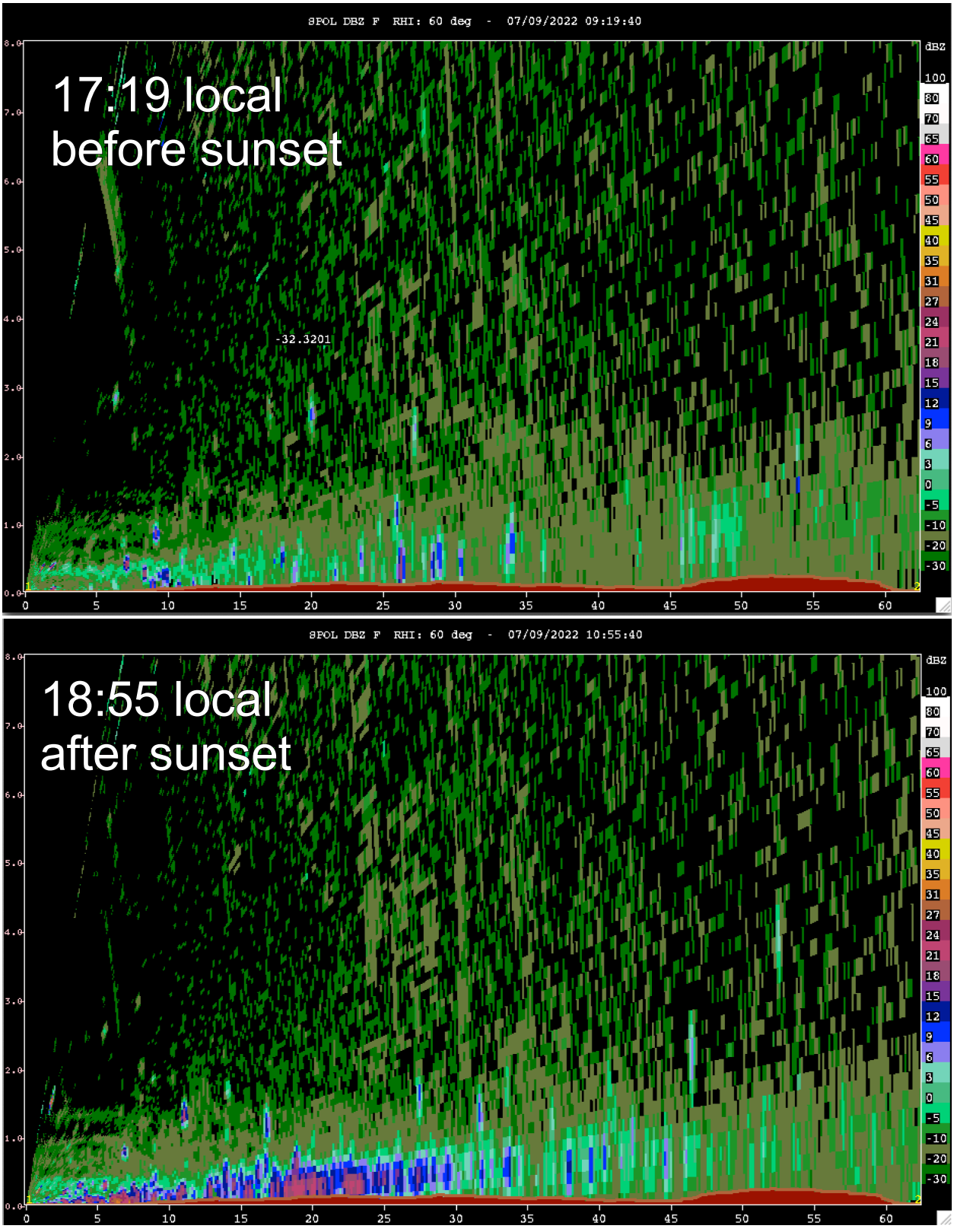

Figure 23: RHI of insect reflectivity. Top: before sunset. Bottom: after sunset..

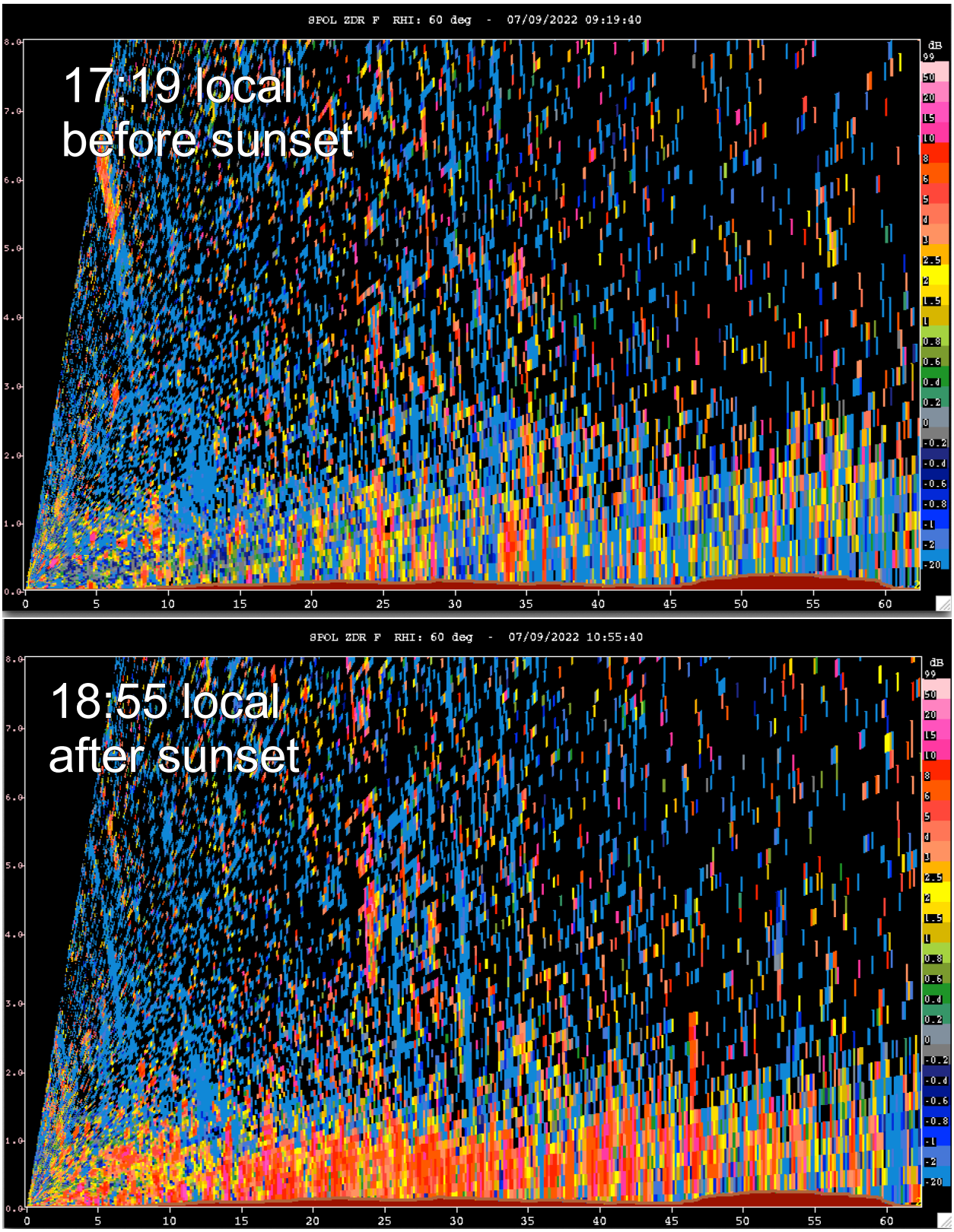

Figure 24: RHI of insect Z_{DR}, filtered. Top: before sunset. Bottom: after sunset..

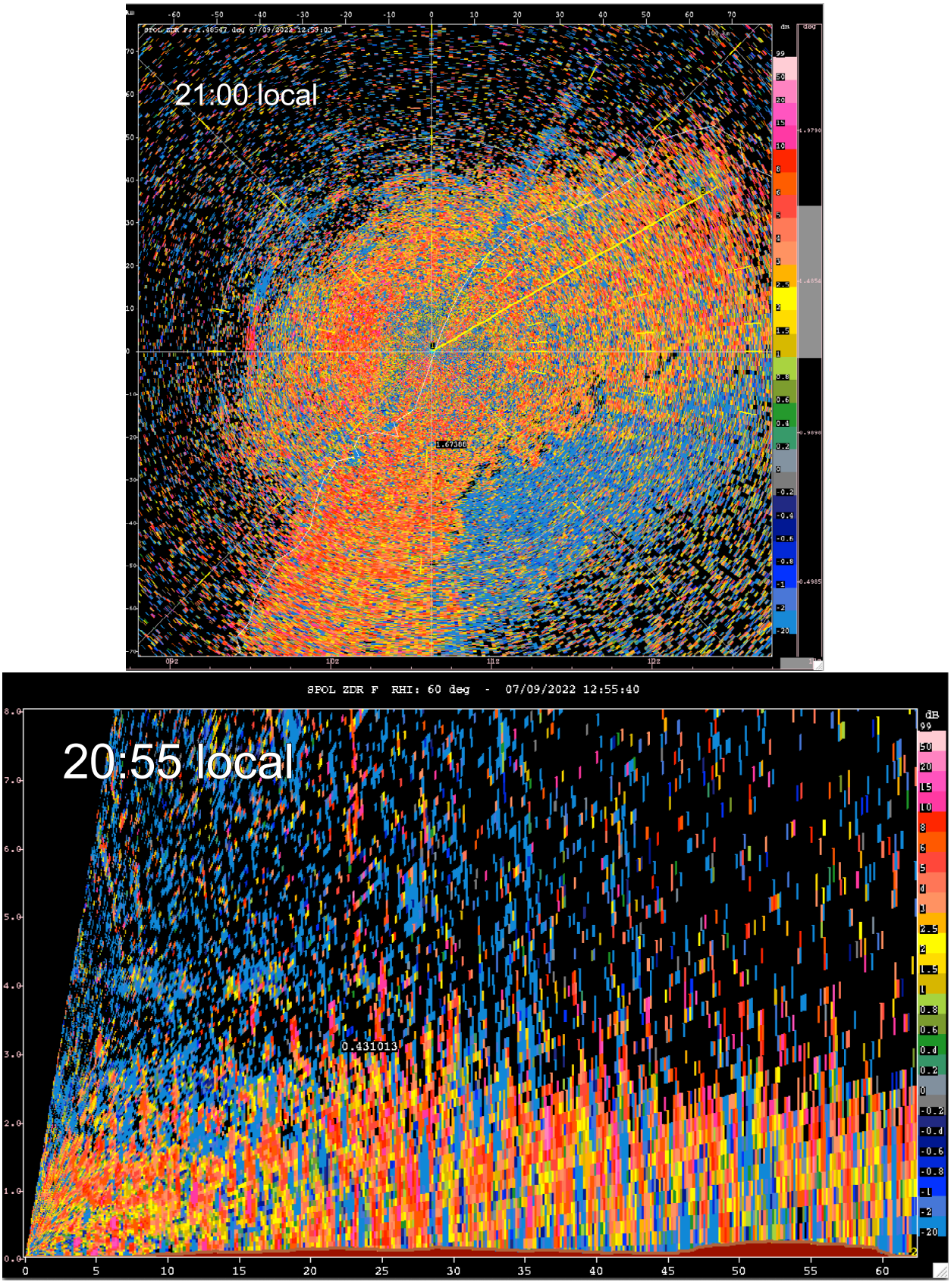

Figure 25: Insect Z_{DR} at about 9 PM local. Top: PPI Z_{DR} filtered. Bottom: RHI Z_{DR} filtered. Insects and birds have now moved over the ocean and are seen at higher altitudes.

9 Sidelobe Bias Effects

Antenna pattern sidelobes effects are evident throughout the PRECIP data set especially in low reflectivity areas. An easy place to see this is in RHIs in clear air well above ground level. Sidelodes "see" the ground clutter and vertical going streaks of constant distance from the radar are easily seen. Much of this clutter reflectivity is eliminated by the clutter filter.

Less obvious sidelobe effects are seen in regions of sharp reflectivity gradient where the main lobe of the antenna pattern is looking at very low reflectivity and the sidelobes are illuminating a much higher reflectivity region. Most times this high reflectivity region lies out side of the RHI or PPI plane being viewed thus making the cause of the bias not so obvious. Fortunately for data quality, these low reflectivity sidelobe-biased regions are characterized by low ρ_{HV}, < 0.7 and can thereby be identified and flagged. The Z_{DR} bias is best understood from Fig. 1, a solar scan V - H ($1/Z_{DR}$) pattern. While the V - H difference is fairly constant over the 2° annulus, outside of this, the V - H difference become large with positive values on top and bottom (causing negative Z_{DR} bias), and negative values on the right and left (causing positive Z_{DR} bias). The sidelobe V - H difference is unknown and a quantitative analysis of this bias is difficult.

Three examples of sidelobe caused bias are given next.

9.1 RHI Case

Figure 26 shows RHIs of filtered reflectivity (top), filtered Z_{DR} (middle) and filtered ρ_{HV} without noise correction (bottom). For data quality purposes, not correcting for noise is preferred. For low reflectivity (more specifically low SNR) regions, this correction artificially can make ρ_{HV} very high giving the viewer a false sense that the data is reliable and of high quality. In each panel of Fig. 26 a red line separates the high reflectivity region (to the right) and a low reflectivity region (to the left). The bias in Z_{DR} is evident with both very high Z_{DR} (10 dB or more) and low Z_{DR} (-8 dB and lower). The ρ_{HV} in the lower panel shows very low values in this region thus these are not meteorological signals.

9.2 PPI Case, 4° Elevation

Figure 27 and 28 show a PPI case with reflectivity and Z_{DR} in Fig. 27, top and bottom, respectively, and the accompanying ρ_{HV} in Fig. 28. The region of Z_{DR} bias is indicated by the white ovals. The pink Z_{DR} values are greater that 10 dB. Many times thin lines of high Z_{DR} are seen in front of a high reflectivity storm as is moves creating a Gust front a line of convergence that sweeps up and concentrates insects. This is not the case here. The pink area of Z_{DR} is at or above the freezing level where insects are not found.

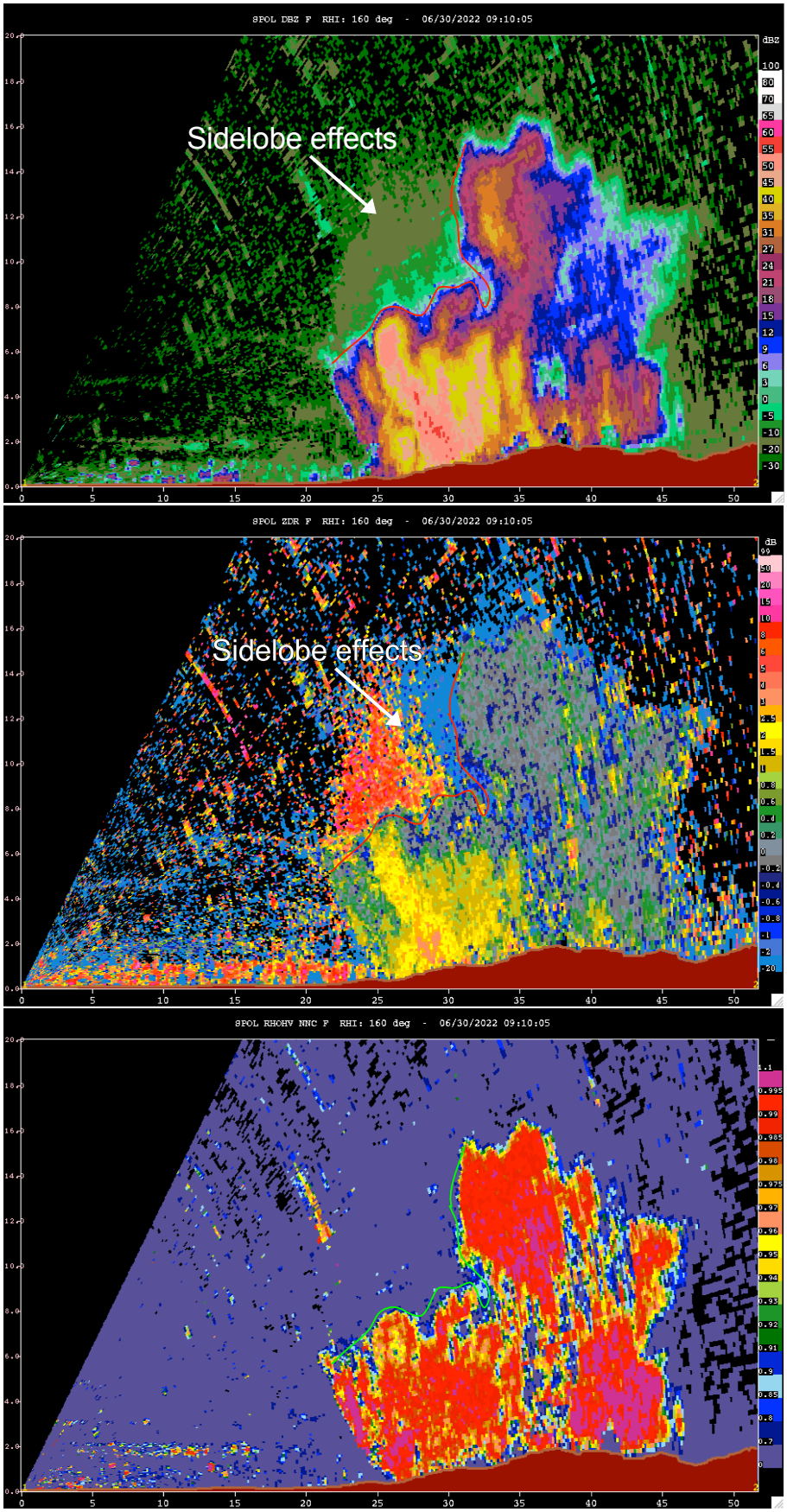

Figure 26: RHI sidelobe bias. Top: reflectivity filtered; middle: Z_{DR} filtered; bottom: ρ_{HV} filtered without noise correction. The red (top, middle) and green (bottom) lines separate the high reflectivity and low reflectivity area with biases

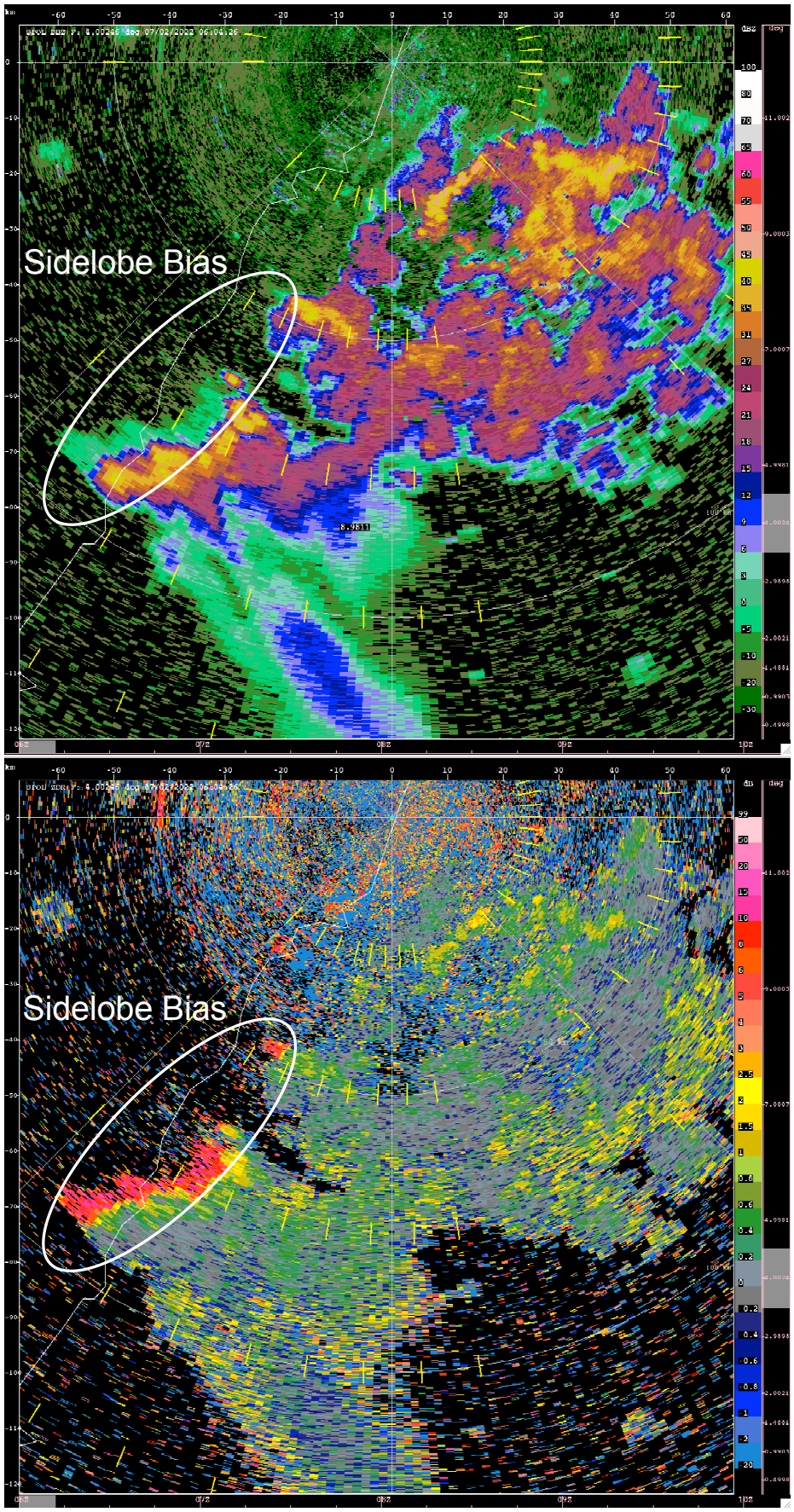

Figure 27: Sidelobe bias. Top: reflectivity filtered at 4° elevation. Bottom: ρ_{HV} filtered. White oval shows biased region. The High Z_{DR} (pink color) is due to sidelobes.

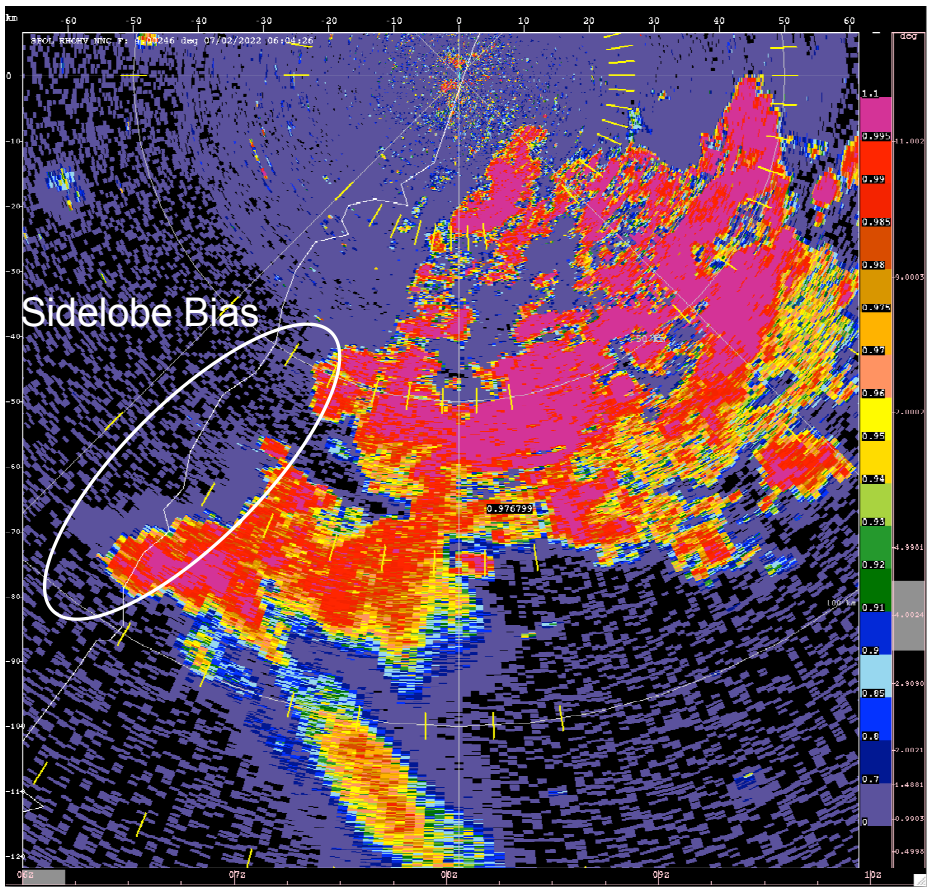

Figure 28: Filtered ρ_{HV} without noise correction. The biased area has very low ρ_{HV}.

9.3 PPI Case 0.5° Elevation

This is an interesting low elevation angle case, 0.5°, where no high reflectivity region is seen. Figure 29 shows the reflectivity on top with Z_{DR} on the bottom. The areas of interest are circled and have very high Z_{DR} with a small area of negative Z_{DR} accompanied by low reflectivity. Figure 29 (top) shows the accompanying ρ_{HV} with very low values in the circled areas. Thus, the signal in the circles is non meteorological. At this low elevation angle it could be argued that insects are a possibility since they too are characterized by low ρ_{HV}. However, Fig. 29 (bottom) shows reflectivity max. in a column thus revealing the high reflectivities in the circled regions. If one examines RHIs through the circled regions, it becomes obvious that the circled regions (at 0.5° elev.) have no direct line of sight to the radar! These regions are blocked by the mountains. Thus, the only possibility is that the sidelobes see the high reflectivities above the circled regions and cause the Z_{DR} and dBZ bias.

10 Sea Clutter and Waves

The reflectivity from the ocean depends on the size of the waves and the tide. Higher winds drive higher waves and cause higher reflectivities. This is more pronounced at high tide. The range extent of the higher reflectivity will also depend on the level of atmospheric super refraction (i.e., AP condition). Figure 31 shows reflectivity from a low wind day (top) and a high wind day (bottom) with significant waves. The reflectivity close to S-Pol is much higher on the high wind day. Figure 32 shows Z_{DR} (top) and ρ_{HV} (bottom) corresponding to Fig. 31 (bottom). Z_{DR} is quite negative and doesn't seem to be affected by the wind. The ρ_{HV} is less that 0.7 where the waves are.

11 Bragg Scatter

Figure 33 shows an example of Bragg scatter on 11 July at 21:32 UTC at 270°. Bragg scatter is characterized by low reflectivity (< 0 dBZ), near unity ρ_{HV} and zero Z_{DR}. Since Bragg scatter is caused by turbulence, on the order of half the radar wavelength, Bragg is seen many times in regions of horizontal shear as demonstrated by the velocity and spectrum width RHIs. As compared to PECAN data, not much Bragg scatter was observed during PRECIP though we did not do an extensive search

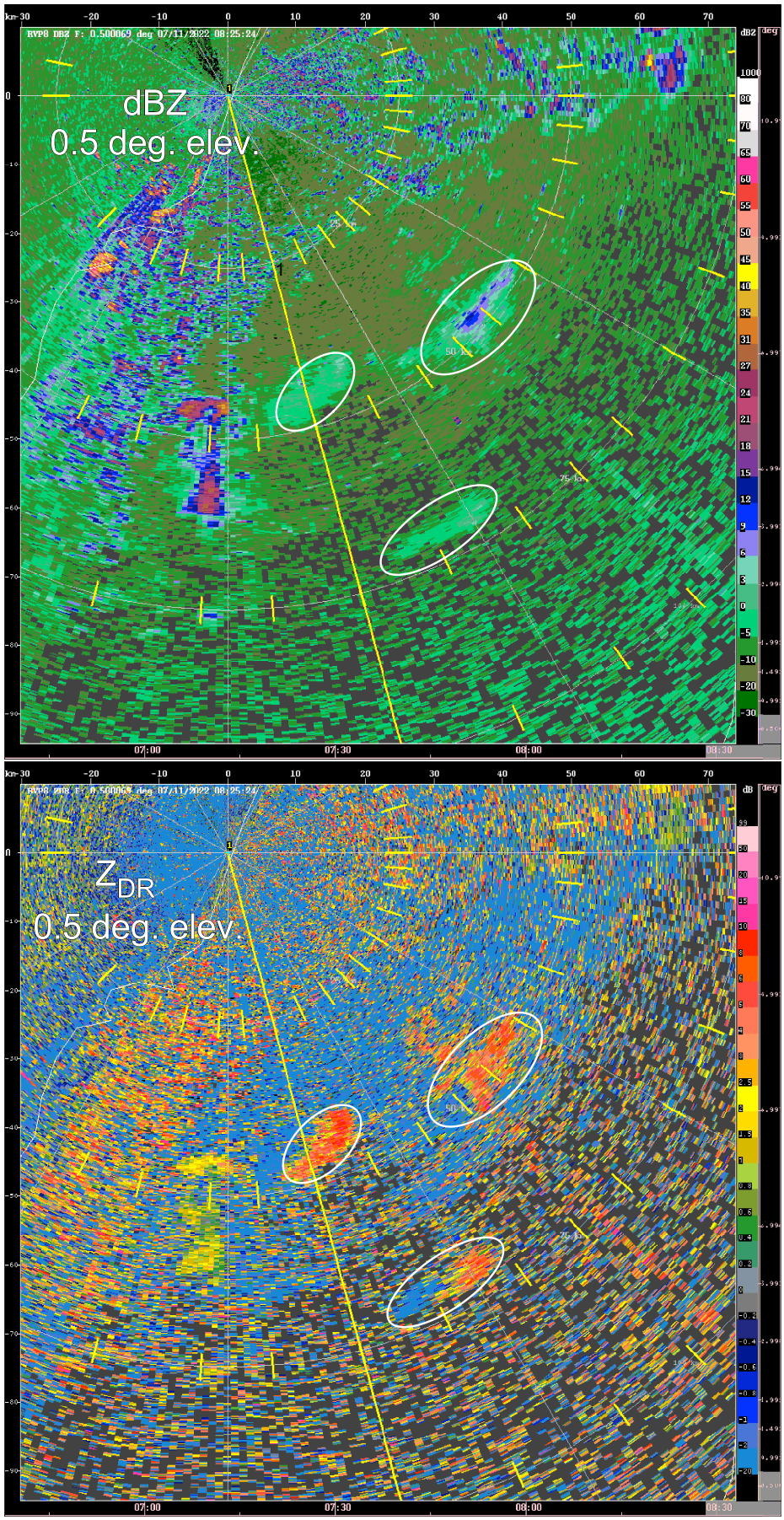

Figure 29: Sidelobe bias effects. Elevation is 0.5°. Top: reflectivity; bottom: Z_{DR}. Bias is seen in the white circled areas.

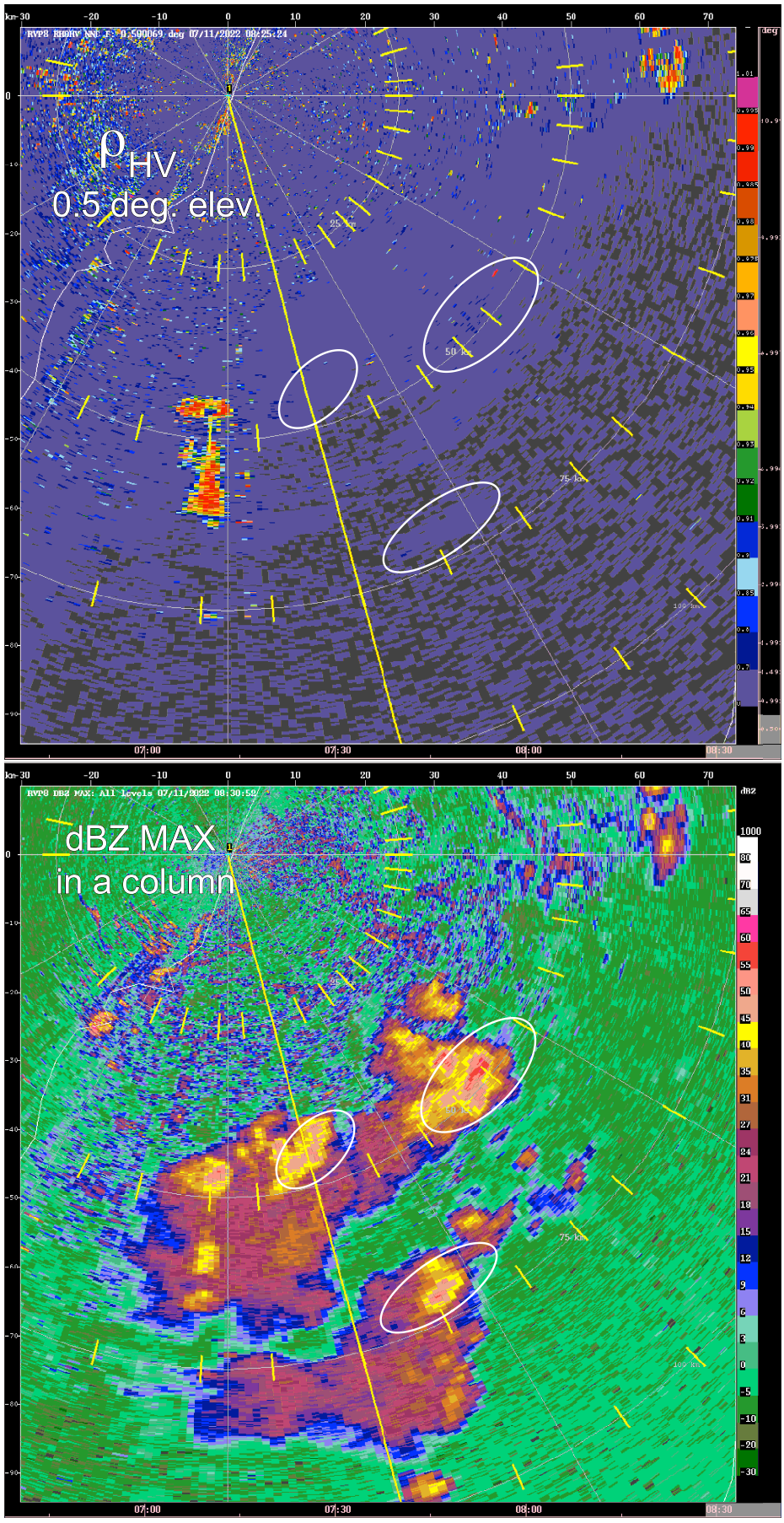

Figure 30: Sidelobe bias effects corresponding to Fig. 29. Top: ρ_{HV} filtered at 0.5° elevation. Bottom: Max. dBZ in a column revealing the high reflectivity above.

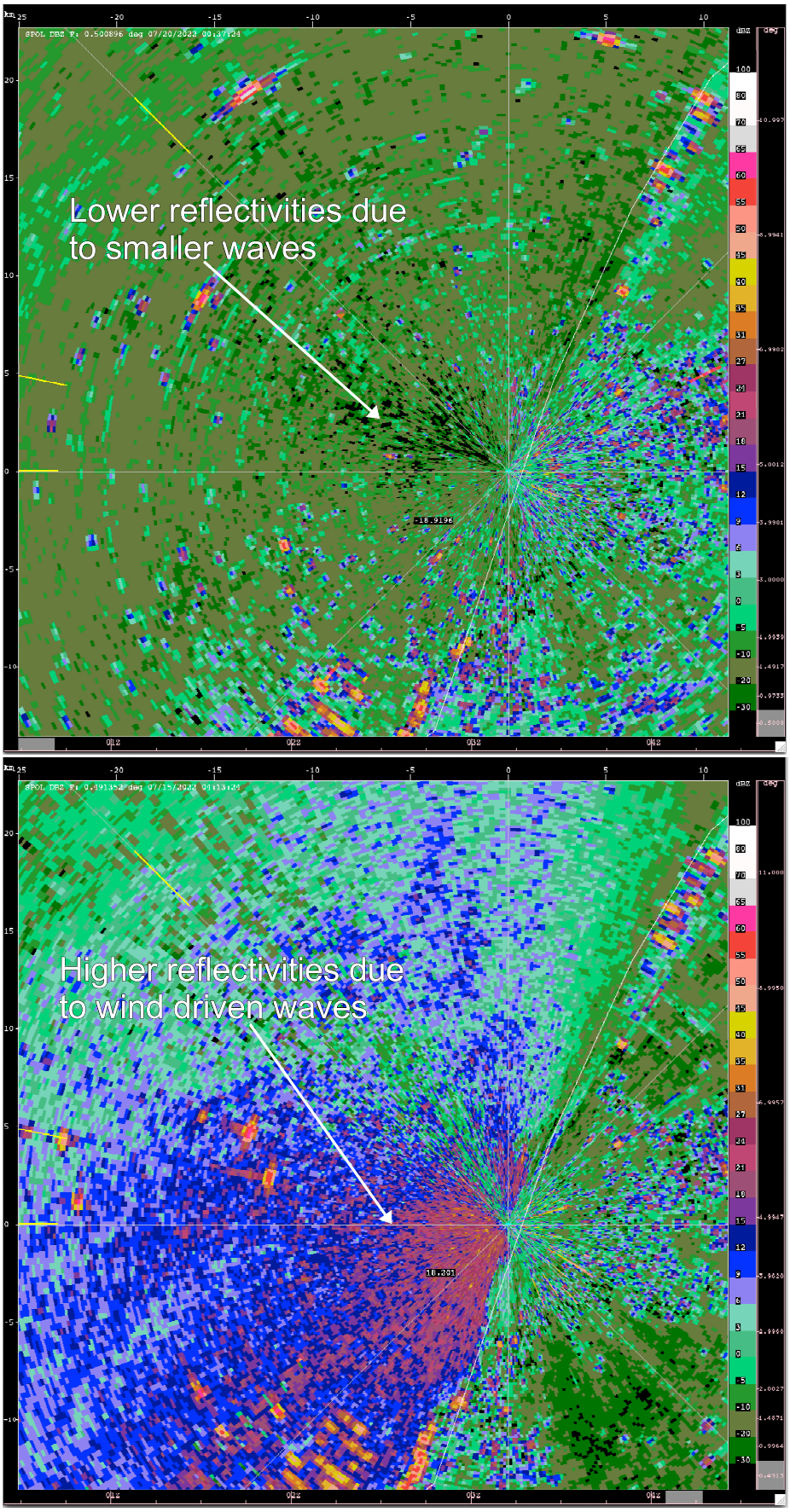

Figure 31: Sea clutter reflectivity. Top: exemplifies low winds days and small waves; Bottom: exemplifies high wind days with larger waves. The sea clutter reflectivity would be higher at high tide.

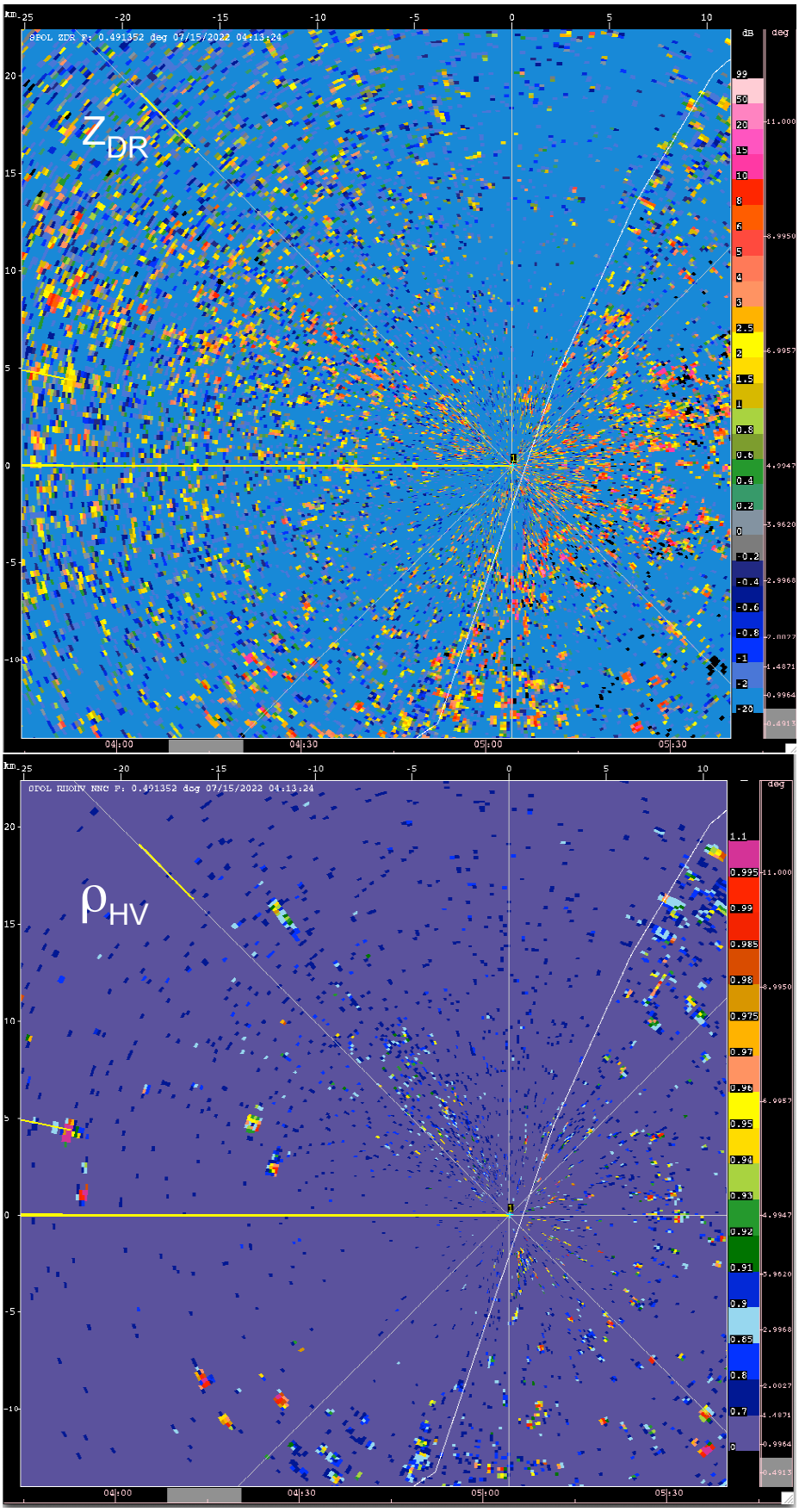

Figure 32: The Z_{DR} (top) and ρ_{HV} (bottom) corresponding to Fig. 31, top panel. The Z_{DR} is quite negative and the ρ_{HV} is low where the waves are.

of the PRECIP data set. Bragg scatter regions can be used to estimate the Z_{DR} bias as is done by NEXRAD (Hubbert, 2017). As can be seen in Fig. 33, Z_{DR} is approximately zero in the Bragg region. Bragg scatter and scatter from cloud droplets are identical. Thus to be certain that Bragg scatter rather than cloud scatter is present, visual observations of the sky are needed.

12 Aligned Ice Crystals Above the Melting Layer

Aligned ice crystals in the ice phase were ubiquitous in PRECIP, which is a common feature of storms. The ice crystals fall and are aligned by aerodynamics. In this case, the ice crystals' principal axes are aligned in the H and V principal planes thus causing positive Z_{DR} and K_{DP}. If an electric field is present, the ice crystals' principal axes can have a mean canting angle away from H and V. Shown in Fig. 34 is an RHI example of aligned ice crystals from 7 June 2333 UTC at 204° azimuth. The total maximum amount of accumulated ϕ_{DP} is about 40°, which is considerable in ice. Z_{DR} is predominately positive in the increasing ϕ_{DP} region at about 0.75 to 1 dB.

For PRECIP, S-Pol operated in simultaneous H and V transmit (SHV) mode as does NEXRAD. If ice crystals are canted due to an electric field, biases in Z_{DR} can be induced. This makes interpretation of Z_{DR} in the ice phase difficult (Ryzhkov and Zrnić, 2007). For more information on the interpretation of Z_{DR} and ϕ_{DP} in the ice phase see Hubbert et al. (2010b,a).

Acknowledgment Thanks to all the people that made S-Pol at PRECIP 2022 a success!

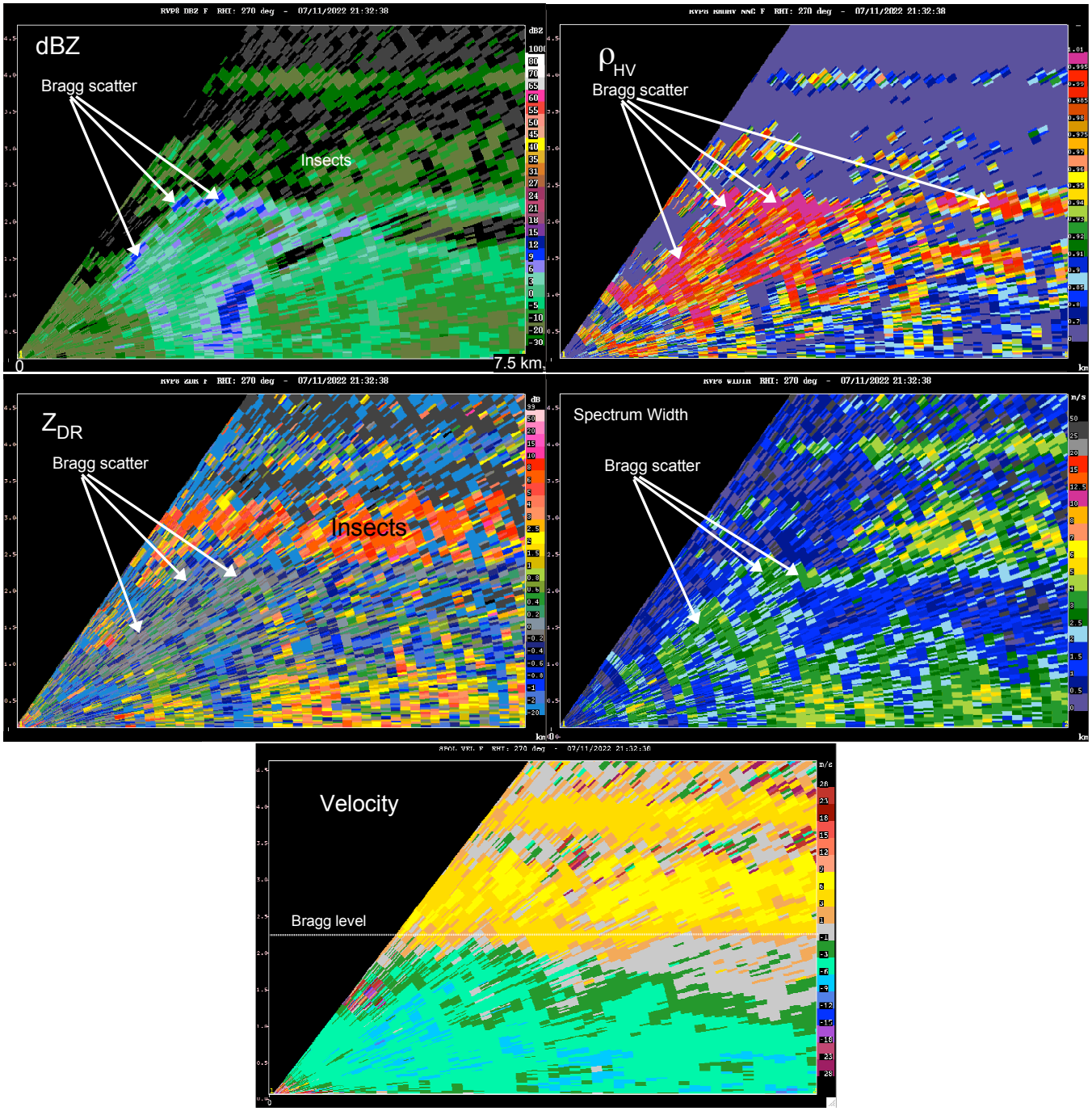

Figure 33: Bragg scatter RHI from 11 July at 21:32 UTC at 270° azimuth. Bragg scatter region usually displays very high ρ_{HV} (not corrected for noise) values if the SNR is high. Range axis is 0 to 7.5 km, height is 0 to 4.5 km.

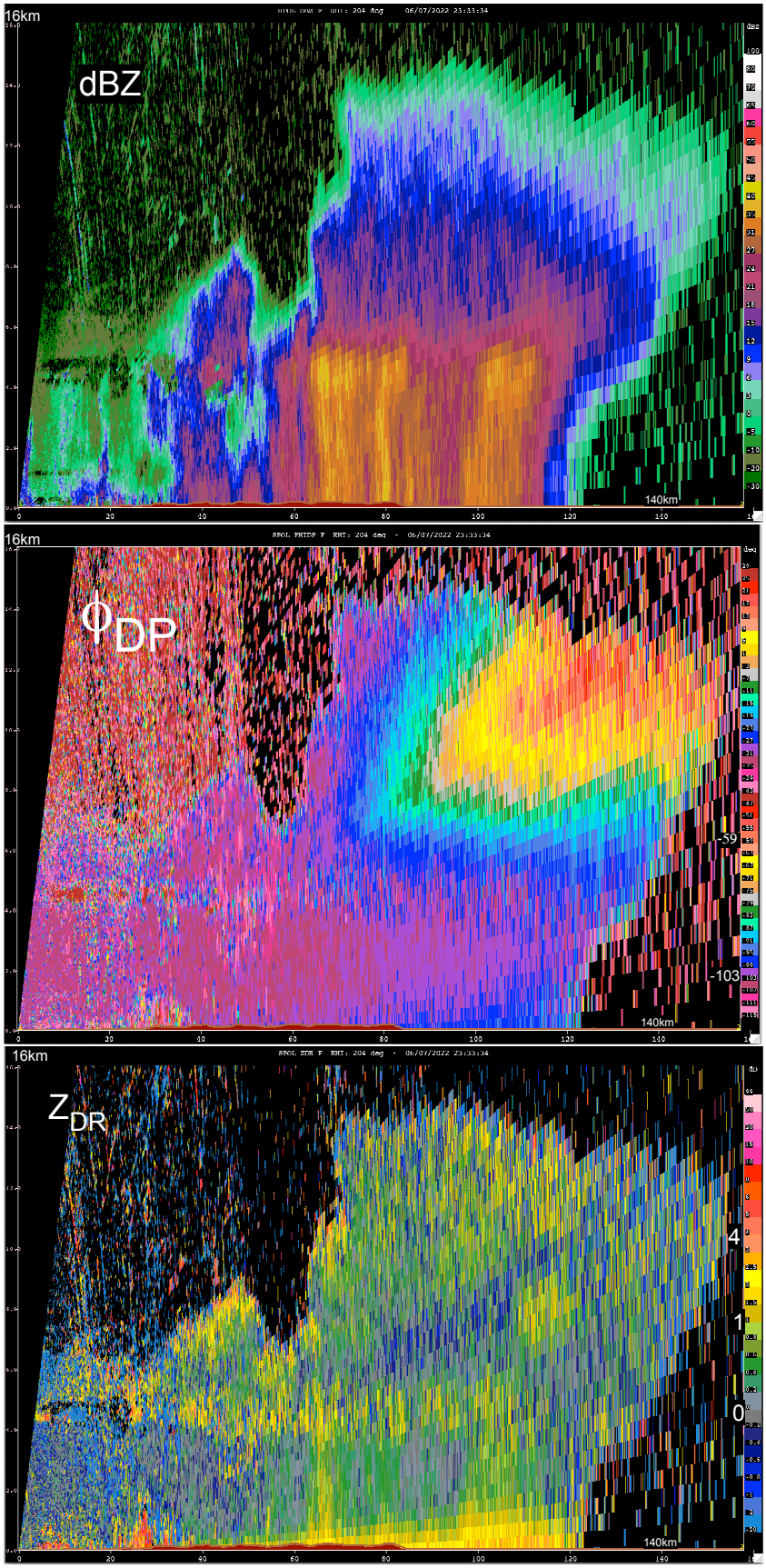

Figure 34: An example of aligned ice crystals in ice phase.

References

Chilson, P. B., et al., 2012: Partly cloudy with a chance of migration: weather, radars, and aeroecology. *Bulletin of the American Meteorological Society*, **93**, 669–686.

Drake, V. A. and D. R. Reynolds, 2012: *Radar Entomology*: *Observing Insect Flight and Migration*. CAB International, 489 pp., iSBN:978 1 84593 556 6.

Hu, G., K. S. Lim, N. Horvitz, S. J. Clark, D. R. Reynolds, N. Sapir, and J. W. Chapman, 2016: Mass seasonal bioflows of high-flying insect migrants. *Science*, **354**, 1584–1587.

Hubbert, J., S. Ellis, M. Dixon, and G. Meymaris, 2010a: Modeling, error analysis and evaluation of dual polarization variables obtained from simultaneous horizontal and vertical polarization transmit radar. Part II: Experimental data. *J. Atmos. Oceanic Technol.*, **27 (10)**, 1599–1607.

Hubbert, J. C., 2017: Differential reflectivity calibration and antenna temperature. *J. Atmos. Oceanic Technol.*, doi.org/10.1175/JTECH-D-16-0218.1.

Hubbert, J. C., W. Deierling, and P. Kennedy, 2015: Detection of electrification with the co-to-cross correlation coefficient with storm microphysics analysis. *Proceedings of 37th Conference on Radar Meteorology*, Norman, OK, American Meteorological Society.

Hubbert, J. C., S. Ellis, W.-Y. Chang, M. Dixon, and Y.-C. Liou, 2014a: X-band polarimetric observations of cross-coupling in the ice phase of convective storms in taiwan. *J. of Applied Meteor. and Clim.*

Hubbert, J. C., S. Ellis, W.-Y. Chang, S. Rutledge, and M. Dixon, 2014b: Microphysical interpretation of S-band simultaneous horizontal and vertical polarization transmit radar data. *J. of Applied Meteor.and Clim.*

Hubbert, J. C., S. Ellis, M. Dixon, and G. Meymaris, 2010b: Modeling, error analysis and evaluation of dual polarization variables obtained from simultaneous horizontal and vertical polarization transmit radar. Part I: Modeling and antenna errors. *J. Atmos. Oceanic Technol.*, **27 (10)**, 1583–1598.

Hubbert, J. C., J. W. Wilson, T. M. Weckwerth, S. M. Ellis, M. Dixon, and E. Loew, 2018: S-pol's polarimetric data reveals detailed storm features (and insect behavior). *Bull. Amer. Meteor. Soc.*, 2045–2060, https://doi.org/10.1175/BAMS-D-17-0317.1.

Kurdzo, J., E. R. Williams, D. J. Smalley, B. J. Bennett, D. C. Patterson, M. S. Veillette, and M. F. Donovan, 2018: Polarimetric observations of chaff using the WSR-88D network. *J. App. Meteor. Clim.*, **57**, 1063–1081.

Lang, T. J., S. A. Rutledge, and J. L. Smith, 2004: Observations of quasi-symmetric echo patterns in clear air with the CSU-CHILL polarimetric radar. *J. Atmos. Oceanic Technol.*, **21**, 1182–1189, doi 10.1175/1520-0426(2004)021<1182 OOQEPI>2.0.CO;2.

Long, M. W., 2001: *Radar Reflectivity of Land and Sea*. Artech House, Boston–London, 534 pp.

Melnikov, V. M., M. J. Istok, and J. K. Westbrook, 2015: Asymmetric radar echo patterns from insects. *J. Atmos. Oceanic Technol.*, **52**, 2276–2285, doi:10.1175/JTECH-D-13-00247.1.

Mueller, E. A. and R. P. Larken, 1985: Insects observed using dual-polarization radar. *J. Atmos. Oceanic Tech.*, **2**, 49–54.

Ryzhkov, A. and D. Zrnić, 2007: Depolarization in ice crystals and its effect on radar polarimetric measurements. *J. Atmos. Oceanic Tech.*, **24**, 1256–1267.

Vivekanandan, J., J. Hubbert, S. Ellis, and J. Wilson, 2013: Radar observations and radar model computations of biological scatterers. *36th Conf. on Radar Meteorology*, Breckenridge, CO, Amer. Meteor. Soc., 13A.1, available online at https://ams.confex.com/ ams/36Radar/webprogram/Paper228792.html.

Wilson, J., T. Weckwerth, J.Vivekanandan, R. Wakimoto, and R. Russell, 1994: Boundary layer clear-air radar echoes: Origin of echoes and accuracy of derived winds. *J. Atmos. Ocean. Tech.*, **11**, 1184–1206.

Zrnić, D. S. and A. V. Ryzhkov, 1998: Observations of insects and birds with a polarimetric radar. *EEE Trans. Geosci. Remote Sens.*, **36**, 661–668, doi 10.1109/36.662746.